The Astrophysical Journal, 796:14 (17pp), 2014 November 20 doi:10.1088/0004-637X/796/1/14
© 2014. The American Astronomical Society. All rights reserved. Printed in the U.S.A.

DIFFUSE γ-RAY EMISSION FROM GALACTIC PULSARS

F. Calore[1], M. Di Mauro[2,3], and F. Donato[2]
[1] GRAPPA Institute, University of Amsterdam, Science Park 904, 1090 GL Amsterdam, The Netherlands; f.calore@uva.nl
[2] Dipartimento di Fisica, Torino University and INFN, Sezione di Torino, Via P. Giuria 1, I-10125 Torino, Italy; mattia.dimauro@to.infn.it
[3] Laboratoire d'Annecy-le-Vieux de Physique Théorique (LAPTh), Univ. de Savoie, CNRS, B.P.110, F-74941 Annecy-le-Vieux, France; donato@to.infn.it
Received 2014 June 27; accepted 2014 September 17; published 2014 October 30

ABSTRACT

Millisecond pulsars (MSPs) are old fast-spinning neutron stars that represent the second most abundant source population discovered by the Large Area Telescope (LAT) on board the *Fermi Gamma-ray Space Telescope* (*Fermi*). As guaranteed γ-ray emitters, they might contribute non-negligibly to the diffuse emission measured at high latitudes by *Fermi*-LAT (i.e., the Isotropic Diffuse γ-Ray Background (IDGRB)), which is believed to arise from the superposition of several components of galactic and extragalactic origin. Additionally, γ-ray sources also contribute to the anisotropy of the IDGRB measured on small scales by *Fermi*-LAT. In this manuscript we aim to assess the contribution of the unresolved counterpart of the detected MSPs population to the IDGRB and the maximal fraction of the measured anisotropy produced by this source class. To this end, we model the MSPs' spatial distribution in the Galaxy and the γ-ray emission parameters by considering observational constraints coming from the Australia Telescope National Facility pulsar catalog and the Second *Fermi*-LAT Catalog of γ-ray pulsars. By simulating a large number of MSP populations through a Monte Carlo simulation, we compute the average diffuse emission and the anisotropy 1σ upper limit. We find that the emission from unresolved MSPs at 2 GeV, where the peak of the spectrum is located, is at most 0.9% of the measured IDGRB above 10° in latitude. The 1σ upper limit on the angular power for unresolved MSP sources turns out to be about a factor of 60 smaller than *Fermi*-LAT measurements above 30°. Our results indicate that this galactic source class represents a negligible contributor to the high-latitude γ-ray sky and confirm that most of the intensity and geometrical properties of the measured diffuse emission are imputable to other extragalactic source classes (e.g., blazars, misaligned active galactic nuclei, or star-forming galaxies). Nevertheless, because MSPs are more concentrated toward the galactic center, we expect them to contribute significantly to the γ-ray diffuse emission at low latitudes. Because, along the galactic disk, the population of young pulsars overcomes in number that of MSPs, we compute the γ-ray emission from the whole population of unresolved pulsars, both young and millisecond, in two low-latitude regions: the inner Galaxy and the galactic center.

Key word: gamma rays: diffuse background

Online-only material: color figures

1. INTRODUCTION

A guaranteed component of the γ-ray sky is represented by a faint and (almost) isotropic emission at latitudes $|b| \geqslant 10^\circ$. Such an Isotropic Diffuse γ-Ray Background (IDGRB) was first suggested by the OSO-3 satellite (Kraushaar et al. 1972) and then measured by SAS-2 (Fichtel et al. 1975) and EGRET (Sreekumar et al. 1998). The Large Area Telescope (LAT) on board the *Fermi Gamma-ray Space Telescope* (*Fermi*) has published a precise measurement of the IDGRB (Abdo et al. 2010b) in the 200 MeV–100 GeV energy range, describing it with a single power law with an index of -2.41 ± 0.15. Recently, the *Fermi*-LAT γ-ray data have unveiled in the IDGRB an anisotropy signal at small scales (Ackermann et al. 2012a). Thus, while being isotropic on large scales, the IDGRB presents fluctuations at $\theta \leqslant 2^\circ$, that are consistent with a population of point-like sources. One of the main puzzles for current γ-ray astrophysics is to understand the origin of this emission and its anisotropy, giving a coherent picture for those two measurements.

Typically, the IDGRB is thought to arise from the superposition of several contributions that can be ascribed to two main categories (Calore et al. 2012): the emission from the unresolved counterpart of known γ-ray point source emitters and the emission from diffuse processes involving interstellar gas and radiation fields. As for the former, extragalactic and galactic source classes may participate in producing the measured IDGRB flux. In particular, active galactic nuclei (AGNs), which represent the population with the largest detected counterpart, are believed to explain most of the IDGRB, as it has been estimated, for example, in Abdo et al. (2010a), Ajello et al. (2012, 2014), Di Mauro et al. (2014b), and Abazajian et al. (2011) for blazars (BL Lac objects and FSRQs) and Inoue (2011) and Di Mauro et al. (2014a) for misaligned AGNs. Another extragalactic source of guaranteed diffuse emission is the unresolved population of star-forming galaxies, normal and starburst, that may even dominate the emission at few GeV because of the hadronic origin of the γ rays (Ackermann et al. 2012b; Tamborra et al. 2014).

The second most abundant population detected by the LAT is represented by galactic young pulsars and millisecond pulsars (MSPs). In particular, pulsars were established as γ-ray emitters by the first observations of *Fermi*-LAT. Since the start of the mission, the number of pulsars detected by LAT has increased significantly and the most up-to-date catalog of such objects is the Second *Fermi*-LAT Catalog of γ-ray pulsars (2FPC; Abdo et al. 2013).

We mention here that truly diffuse processes may also contribute to the IDGRB. Among others, we note the γ-ray production from the interaction of ultra-high-energy cosmic rays with the cosmic microwave background (Kalashev et al. 2009; Berezinsky et al. 2011), the emission originating from photons up-scattered through an inverse Compton process by

a population of highly relativistic electrons created during clusters mergers (Blasi et al. 2007), and γ rays produced by the annihilation of Dark Matter (DM) particles in the Milky Way or in external galaxies, e.g., Bergström et al. (1998); Abazajian et al. (2010); Fornasa et al. (2013); Calore et al. (2014); Bringmann et al. (2014).

We do not aim to give an extensive discussion of the different contributions to the high-latitude diffuse emission, and we refer to Calore et al. (2012), Bringmann et al. (2014), Di Mauro et al. (2014b), and Cholis et al. (2014) for more detailed explanations. Nevertheless, we stress that in this paper it has been shown that current predictions of the unresolved emission from blazars, misaligned AGNs, star-forming galaxies, and MSPs could fully explain the IDGRB data in the *Fermi*-LAT whole energy range.

This work will focus on the galactic pulsars population and aims to assess the contribution to the IDGRB arising from the unresolved counterpart of this source class. In particular, we are interested in the high-latitude γ-ray flux in the analysis of MSPs instead of young pulsars, because such a population is expected to dominate the γ-ray emission in this region. MSPs are old, rapidly spinning neutron stars (with rotation period $P \leqslant 15$ ms) that are usually found (about 80% of MSPs) in binary systems and accrete matter from a companion (Alpar et al. 1982). Pulsars are believed to emit γ rays from the conversion of their rotational kinetic energy. The initial rotational period (when the pulsar is born) slows down as a consequence of the magnetic-dipole braking (Ng et al. 2014; Lyne 2000). This decline is measured by the time derivative of the period, $\dot{P}$, which is related to the spin period, P, and the surface magnetic field, B (Grégoire & Knödlseder 2013; Faucher-Giguère & Loeb 2010; Abdo et al. 2013):

$$\dot{P} = 9.8 \times 10^{-40} \left(\frac{B}{\mathrm{G}}\right)^2 \left(\frac{P}{\mathrm{s}}\right)^{-1}. \quad (1)$$

As a consequence, the loss energy rate, $\dot{E}$ (i.e., spin-down luminosity), is (Grégoire & Knödlseder 2013):

$$\dot{E} = 4\pi^2 M \frac{\dot{P}}{P^3}, \quad (2)$$

where M is the moment of inertia of the star assumed to be 10^{45} g cm^2 (Grégoire & Knödlseder 2013; Faucher-Giguère & Loeb 2010; Abdo et al. 2013). The spin-down luminosity is then converted with some efficiency into radiation.

For young pulsars that typically have periods of hundreds of ms, the slowing down of the period is rapid and they lose their energy very fast, such that their γ-ray emission is substantially smaller than their older and faster spinning companions. Indeed, assuming that the γ-ray luminosity follows the same relation $L_\gamma \propto \dot{P}^{1/2} P^{-3/2}$ (Faucher-Giguère & Loeb 2010) for all pulsars we can write:

$$\frac{L_\gamma^{\mathrm{MSP}}}{L_\gamma^{\mathrm{young}}} = \left(\frac{\dot{P}_{\mathrm{MSP}}}{\dot{P}_{\mathrm{young}}}\right)^{1/2} \left(\frac{P_{\mathrm{MSP}}}{P_{\mathrm{young}}}\right)^{-3/2}, \quad (3)$$

where typical values for the rotation period P and the time derivative of the period $\dot{P}$ are: $P_{\mathrm{MSP}} = 3$ ms, $P_{\mathrm{young}} = 0.5$ s, $\dot{P}_{\mathrm{MPS}} = 10^{-19}$, and $\dot{P}_{\mathrm{young}} = 10^{-15}$ (Lorimer & Kramer 2004). Therefore, $L_\gamma^{\mathrm{MSP}}/L_\gamma^{\mathrm{young}} \approx 20$ meaning that the average γ-ray luminosity of MSPs is much higher than that of young pulsars. Moreover, due to their age, MSPs are expected to distribute at higher latitudes with respect to young pulsars, which are instead concentrated along the galactic disk, within $|b| = 15^\circ$ (Faucher-Giguère & Loeb 2010; Abdo et al. 2013).

In the present analysis we derive the main characteristics of the pulsar population, namely the spatial distribution and the γ-ray emission parameters, using radio and γ-rays catalogs. We build a model for the pulsar emission that we use to generate Monte Carlo (MC) simulations of the population in order to predict the diffuse γ-ray flux that originated from the non-detected source counterpart and to estimate the relevant theoretical uncertainty affecting our results. The paper is organized as follows. In Section 2 we describe the properties of the galactic MSPs observed in radio and we model their luminosity and spatial distribution performing fits based on radio observations. In Section 3, we move to γ-ray observations and individuate the main spectral and luminosity characteristics of the MSPs as detected by *Fermi*-LAT. With those ingredients, we are able in Section 4 to set up an MC simulation of the MSP population in the Galaxy and generate mock γ-ray emission from the unresolved counterpart of MSPs. Besides computing the diffuse emission coming from this population, we also calculate the anisotropy signal ascribable to such sources. Section 5 is dedicated to the presentation of the results and their discussion. The γ-ray emission from unresolved MSPs at latitudes above 10° is derived in Section 5.1, and we estimate the contribution to the emission in the innermost part of the Galaxy in Section 5.2. Since at low latitudes the population of young pulsars is more abundant than the MSP, we study the spatial and γ-ray emission properties of young sources and take into account the contribution from young pulsars when analyzing low-latitude regions. The conclusions are presented in Section 6.

2. MSP DISTRIBUTION IN THE GALAXY

In order to model the MSP population in our Galaxy, we rely on the Australia Telescope National Facility (ATNF) pulsar catalog (Manchester et al. 2005). It contains 1509 pulsars with published information, which is a huge improvement with respect to the previously available catalog (Taylor & Cordes 1993) containing 558 radio sources. We use the continuously updated online version of the catalog[4] to compile the list of MSPs. In order to build our MSP sample we select, from the whole catalog, those objects with a period $P \leqslant 15$ ms. This upper limit on the P distribution is usually set to distinguish MSPs and young pulsar populations (Abdo et al. 2013; Cordes & Chernoff 1997; Lorimer 2012). We display in Figure 1 the $\dot{P} - P$ plane with all the sources of the ATNF catalog divided into MSPs and young pulsars. We show also the threshold $P = 15$ ms and the *Fermi*-LAT detected MSPs and young pulsars. The majority of MSPs have a period in the range $P \in [1, 10]$ ms, and there is a small number of sources with a period larger than 10 ms. Therefore, the MSP-selected sample weakly depends on the P upper bound. Considering this threshold, we selected 132 MSPs from the ATNF catalog for our analysis. In Figure 2 we show the position of the selected radio sources in the galactic plane, highlighting the Earth position, around which the sources are concentrated. For the sake of comparison, we also show the distribution in the galactic plane of MSPs resolved by the *Fermi*-LAT as reported in the 2FPC catalog (Abdo et al. 2013). Since the distances claimed in the ATNF and 2PFC catalogs differ significantly for several sources, we fixed the distance as reported in Abdo et al. (2013, Table 6) whenever dealing with

[4] http://www.atnf.csiro.au/research/pulsar/psrcat/

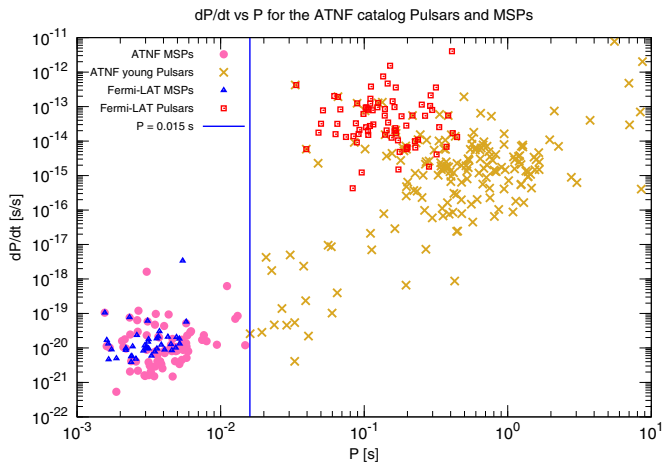

Figure 1. Period P and derivative of the period $\dot{P}$ for the MSPs (pink circles) and young pulsars (gold crosses) selected from the ATNF catalog (Manchester et al. 2005). We also display the *Fermi*-LAT MSPs (blue triangles) and young pulsars (red squares) selected from the 2FPC catalog (Abdo et al. 2013). The solid blue line sets the threshold value $P = 15$ ms, which separates the population into MSPs and young pulsars.

(A color version of this figure is available in the online journal.)

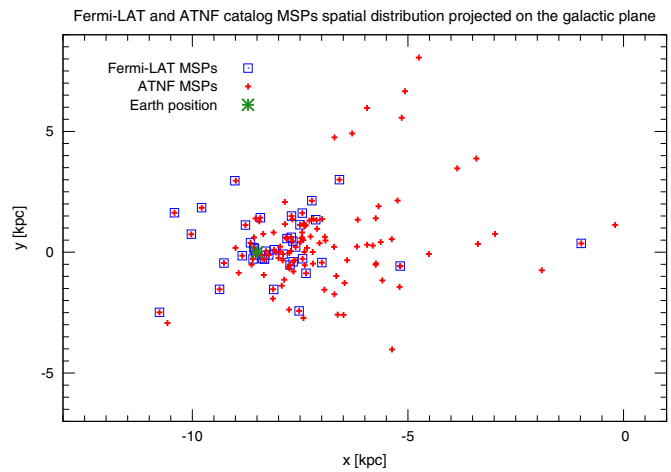

Figure 2. MSP spatial distribution projected on the galactic plane for sources selected from the ATNF catalog (Manchester et al. 2005). The sample has $P \leqslant 15$ ms and is shown with red crosses, while the Earth position is displayed by the green point. For comparison, we also overlap the projected distribution of MSPs resolved by the *Fermi*-LAT and listed in the 2FPC catalog (Abdo et al. 2013, blue squares).

(A color version of this figure is available in the online journal.)

γ-ray MSPs, and fixed it to the value declared in the ATNF catalog for all the other sources.

The physical observables that are directly measured are the period P, the derivative of the period $\dot{P}$, the distance d, the longitude l, and the latitude b. However, the physical parameters that are generally used to derive the emission from pulsars are the surface magnetic field B, the rotation period P, the distance from the galactic plane z, and the distance from the galactic center projected on the galactic plane r, hereafter the radial distance.

The magnetic field can be derived from P and $\dot{P}$ with Equation (1), while z and r are connected to d, l, and b by:

$$z = d \sin b; \;\; r = \sqrt{x^2 + y^2}$$
$$x = d \cos b \cos l - r_{\rm sun}; \;\; y = d \cos b \sin l, \tag{4}$$

where $r_{\rm sun}$ is the distance of the Sun from the galactic center and is fixed at 8.5 kpc (McMillan & Binney 2010; Brunthaler et al. 2011; Gillessen et al. 2009). We use the sample of the 132 MSPs selected from the ATNF catalog to derive the distributions of B, P, r, and z, and we fit them with different functions in order to assess the distribution function of each observable. For the magnetic field B distribution we use a $\log_{10}$ Gaussian function, similar to Siegal-Gaskins et al. (2011); Grégoire & Knödlseder (2013); Faucher-Giguère & Loeb (2010):

$$\frac{dN}{d\log_{10} B} \propto \exp\left(-\frac{(\log_{10} B - \langle \log_{10} B\rangle)^2}{2\sigma^2_{\log_{10} B}}\right), \tag{5}$$

where $\langle \log_{10} B\rangle$ and $\sigma_{\log_{10} B}$ are the mean and the dispersion value of the $\log_{10}$ of the surface magnetic field, respectively. For the period P distribution, we consider a $\log_{10}$ and a linear Gaussian function:

$$\frac{dN}{d\log_{10} P} \propto \exp\left(-\frac{(\log_{10} P - \langle \log_{10} P\rangle)^2}{2\sigma^2_{\log_{10} P}}\right) \tag{6}$$

$$\frac{dN}{dP} \propto \exp\left(-\frac{(P - \langle P\rangle)^2}{2\sigma^2_P}\right), \tag{7}$$

where $\langle \log_{10} P\rangle$ ($\langle P\rangle$) and $\sigma_{\log_{10} P}$ (σ_P) are the mean and dispersion values of the $\log_{10}$ (linear) value of the period. On the other hand, we use an exponential and a Gaussian function for the distance from the galactic plane z:

$$\frac{dN}{dz} \propto \exp\left(-\frac{(z - \langle z\rangle)}{z_0}\right), \tag{8}$$

$$\frac{dN}{dz} \propto \exp\left(-\frac{(z - \langle z\rangle)^2}{2\sigma_z^2}\right), \tag{9}$$

where $\langle z\rangle$, σ_z, and z_0 are the mean, dispersion, and width of the z distribution, respectively. Finally, we try to explain the radial distribution r with an exponential and a linear Gaussian function:

$$\frac{dN}{dr} \propto \exp\left(-\frac{(r - \langle r\rangle)}{r_0}\right), \tag{10}$$

$$\frac{dN}{dr} \propto \exp\left(-\frac{(r - \langle r\rangle)^2}{2\sigma_r^2}\right), \tag{11}$$

where $\langle r\rangle$, σ_r, and r_0 are the mean, dispersion, and width of the r distribution, respectively. The best-fit functions turn out to be a $\log_{10}$ Gaussian distribution for the period P, Equation (7), and an exponential for the distance from the galactic plane z, Equation (8), and the radial distance r, Equation (10). The best fit parameters and the 1σ errors are quoted in Table 1. In Figure 3, we display the magnetic field B, period P, distance from the galactic plane z, and radial distance r distributions for the MSPs of our ATNF catalog sample, together with the theoretical expectations of the same quantities using Equations (5)–(11).

We find that the mean value of the $\log_{10}(B/\mathrm{G})$ Gaussian distribution is 8.3. This result is compatible with Hooper et al. (2013), although a lower value for $\langle \log_{10}(B/\mathrm{G})\rangle$ (i.e., 8) has often been assumed, (Siegal-Gaskins et al. 2011; Grégoire & Knödlseder 2013; Faucher-Giguère & Loeb 2010). The rotation

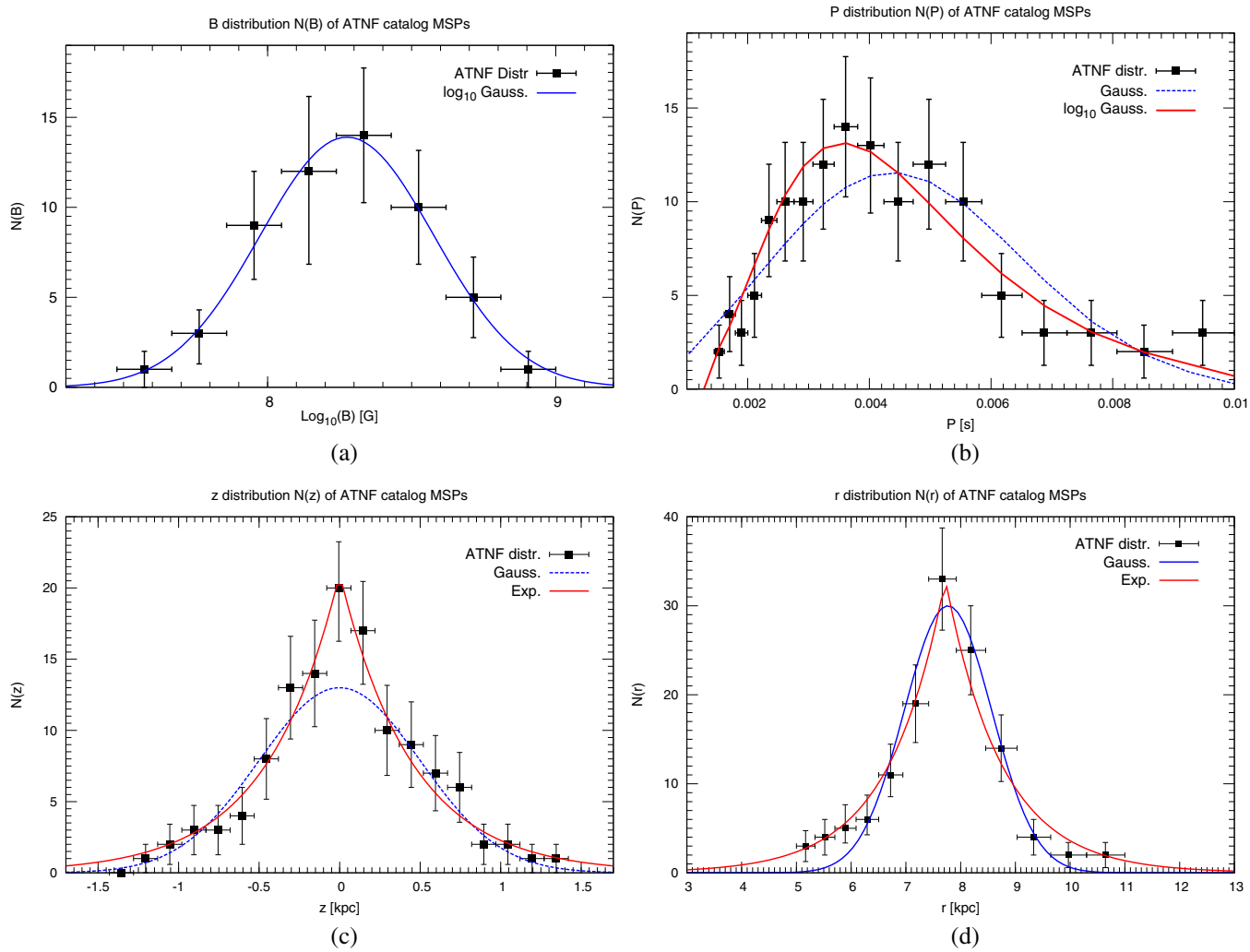

Figure 3. Cumulative distributions from the top left to the bottom right of the magnetic field B, the period P, the distance from the galactic plane z, and the radial distance r for ATNF catalog MSPs. Together with the data we also plot the fitting functions in Equations (5)–(11) for the best-fit parameters.

(A color version of this figure is available in the online journal.)

Table 1
Best fit Parameters for the $\log_{10}$ Gaussian Distribution for the Surface Magnetic Field B and the Period P and the Exponential Distribution for the Distance from the Galactic Plane z and the Radial Distance r for the MSP Population

B	$\langle \log_{10}(B/\mathrm{G})\rangle$	$\sigma_{\log_{10} B}$	P	$\langle \log_{10}(P/\mathrm{s})\rangle$	$\sigma_{\log_{10} P}$
	8.27 ± 0.09	0.30 ± 0.12		-2.54 ± 0.05	0.19 ± 0.03
r	$\langle r\rangle$[kpc]	r_0[kpc]	z	$\langle z\rangle$[kpc]	z_0[kpc]
	7.42 ± 0.28	1.03 ± 0.35		0.00 ± 0.14	0.67 ± 0.11

period distribution turns out to be compatible with a $\log_{10}$ Gaussian,[5] Equation (7) with $\langle \log_{10}(P/\mathrm{s})\rangle = -2.54$. The results for the P distribution represent a novelty with respect to previous works. Indeed, in Siegal-Gaskins et al. (2011); Grégoire & Knödlseder (2013); Faucher-Giguère & Loeb (2010) a power law was used, $N(P) \propto P^{-\alpha}$. This assumption is based on the results of Cordes & Chernoff (1997), where the P distribution of 22 MSPs is fitted with a power law. It is clearly shown in Figure 3 that the distribution at small values of P (1–4 ms) is not compatible with a power law; rather, it is explained fairly well by a Gaussian. At a few ms there is a drop in the distribution because the number of sources with such a small rotation period decreases. This trend (less sources at smaller P) is not an experimental bias associated to the difficulty of detecting such small rotation periods. Actually, the uncertainties on the measurement of P from radio telescopes are much smaller than a few ms (see, e.g., Keith et al. 2011; Burgay et al. 2013; Lange et al. 2001). Thus the decreasing shape at small rotation periods is physical and not due to an experimental bias.

As for the z distribution, an exponential function with $z_0 = 0.67$, Equation (8), fits the data well, as it was derived in Levin et al. (2013); Story et al. (2007) for MSPs. Similarly, the result for the r distribution (i.e., an exponential with $\langle r\rangle \sim 8$ kpc, Equation (11)), is in agreement with the previous literature (Levin et al. 2013; Story et al. 2007). As one can see in Figure 3, the radial distance distribution is not centered in zero, but peaks at ∼8 kpc. This is due to a bias in the detection of pulsars. The displacement $\langle r\rangle$ corresponds to the distance of the Earth from the galactic center, meaning that most of the sources should be placed around the Earth. This is exactly what we show in the map of Figure 2, where the location of the ATNF MSPs in the

[5] We obtain that a $\log_{10}$ Gaussian gives a reduced $\chi^2/d.o.f. = 0.21$, while $\chi^2/d.o.f. = 0.28$ for a linear Gaussian. Additionally, we notice that when increasing the MSP maximal period up to 30 ms, the sample is contaminated by the low-period young pulsars. This high-period tail in the MSP's period distribution makes both parameterizations badly fitted.

galactic plane displays a clustering around the Earth position. This result indicates that the closer the sources are to us, the more easily they are detected. This thus represents an experimental bias we have to take into account when dealing with the radial distribution.

Models of the birth and the evolution of radio pulsars (Lorimer et al. 2006; Faucher-Giguere & Kaspi 2006; Yusifov & Kucuk 2004; Faucher-Giguère & Loeb 2010) have found that evolved distributions of pulsars peak at about 3–4 kpc away from the galactic center in the direction of the Earth. Nevertheless, MSPs with typical ages of 1 Gyr or more (Manchester et al. 2005) are expected to have completed many orbits of the Galaxy. The position of such old sources is therefore believed to be uncorrelated with the birth position and the evolved distribution (Faucher-Giguère & Loeb 2010). For this reason, the radial distribution is usually centered in the galactic center $\langle r \rangle = 0$ kpc and modeled with an exponential distribution (e.g., in Story et al. 2007):

$$\frac{dN}{dr} \propto \exp\left(-\frac{r}{r_0}\right), \tag{12}$$

where r_0 is the radial distance width, or with a Gaussian density profile Faucher-Giguère & Loeb (2010):

$$\frac{dN}{dr} \propto \exp\left(-\frac{r^2}{2\sigma_r^2}\right), \tag{13}$$

with σ_r as the distance dispersion. We adopt in the rest of the paper a radial distribution given by Equation (13) with $\sigma_r = 10$ kpc and quantify in the Appendix the uncertainty on the diffuse γ-ray emission given by the choice of other radial distributions.

3. THE POPULATION OF γ-RAY MSPS

The first discovery of a radio MSP dates back to 1982 (Backer et al. 1982). Since then, the studies on this new source class were focused on radio emission, although it was suddenly realized that MSPs could efficiently shine in γ ray as well (Usov 1983).

Before the *Fermi*-LAT operation, only few radio-loud young pulsars were detected in γ ray, while MSP γ-ray emission was finally confirmed by the LAT observations (Abdo et al. 2009). The 2FPC (Abdo et al. 2013) lists 117 γ-ray pulsars detected during the first 3 years of the mission. The 117 pulsars are classified into 3 groups: MSPs, young radio-loud pulsars, and young radio-quiet pulsars. Out of the γ-ray pulsars in this catalog, roughly half (41 young pulsars and 20 MSPs) were already known in radio and/or X-rays. The remaining pulsars were discovered by or with the aid of the LAT, with 36 being young pulsars found in blind searches of LAT data, and the remaining ones being MSPs found in radio searches of unassociated LAT sources. The pulsars of the 2FPC are thus divided into 77 young pulsars and 40 MSPs. All young pulsars except one have latitude $|b| \leqslant 15^\circ$, whereas 31 MSPs (out of 40) have $|b| \geqslant 10^\circ$, mainly because of the poor sensitivity to MSP detection in the inner part of the Galaxy (see Figure 17 of Abdo et al. 2013).

Further studies of the 2FPC and multi-wavelengths analyses shed light on the nature of the γ-ray emission. The spectral cutoff shown by most sources at few GeV is consistent with curvature radiation as the dominant γ-ray production mechanism: electrons and positrons emit γ rays as a consequence of their acceleration along magnetic field lines by the rotationally induced electric field. Inverse Compton (IC) scattering could also participate as an alternative emission mechanism, mainly from synchrotron seed photons (self-synchrotron Compton, SSC). In this case, no strong cutoff at GeV energies is present, making curvature radiation more likely (Kerr & Fermi-LAT Collaboration 2013). Nevertheless, part of the very high-energy emission of the Crab pulsar, whose flux has been measured at $E \geqslant 100$ GeV from VERITAS (VERITAS Collaboration 2011), MAGIC (Magic Collaboration 2011, 2012), and HESS (Aharonian et al. 2006), is believed to arise from IC processes (Lyutikov et al. 2012). From γ-ray studies it is also possible to infer where the emission takes place; observations currently favor the outer magnetosphere location, but the full radiation model is still a matter of debate (see Johnson et al. 2014; Ng et al. 2014 for an updated analysis).

We consider the sample of MSPs as reported in the 2FPC. The spectral energy distribution is fitted by a power law with an exponential cutoff in the form:

$$\frac{dN}{dE} = K\left(\frac{E}{E_0}\right)^{-\Gamma} \exp\left(-\frac{E}{E_{\rm cut}}\right), \tag{14}$$

where K is a normalization factor, Γ is the photon spectral index, and $E_{\rm cut}$ is the energy cutoff. For convenience, we quote in Table 2 the main parameters of those 40 objects: association name, galacto-centric longitude l and latitude b, photon flux F_γ integrated between 100 MeV and 100 GeV, spectral index Γ, and cutoff energy $E_{\rm cut}$.

Spectral index and cutoff energy distributions are consistent with a Gaussian function:

$$\frac{dN}{d\Gamma} = \exp\left(\frac{(\Gamma - \langle\Gamma\rangle)^2}{2\sigma_\Gamma{}^2}\right), \tag{15}$$

$$\frac{dN}{d\tilde{E}_{\rm cut}} = \exp\left(\frac{(\tilde{E}_{\rm cut} - \langle\tilde{E}_{\rm cut}\rangle)^2}{2\sigma^2_{\tilde{E}_{\rm cut}}}\right), \tag{16}$$

where $\tilde{E}_{\rm cut} \equiv \log_{10}(E_{\rm cut}/{\rm MeV})$. $\langle\Gamma\rangle$ and σ_Γ ($\langle\tilde{E}_{\rm cut}\rangle$ and $\sigma_{\tilde{E}_{\rm cut}}$) are the mean and the dispersion values for the photon index ($\log_{10}$ of the energy cutoff) distribution. Best-fit parameters for the sample in Table 2 (excluding the three sources without spectral information) are $[\Gamma, \sigma_\Gamma] = [1.29, 0.37]$ and $[\tilde{E}_{\rm cut}, \sigma_{\tilde{E}_{\rm cut}}] = [3.38, 0.18]$. Figure 4 shows that the two distributions are well fitted by the functions in Equations (15)–(16).

As for the case of the ATNF catalog sample, we derive the distribution of the quantities r and z for the MSPs detected by the *Fermi*-LAT (Table 2). In order to directly compare the distributions of sources derived from the ATNF and *Fermi*-LAT catalogs, we used the following method. We have renormalized the dN/dr and dN/dz distributions in each bin by taking into account the different number of sources in the two catalogs. The sample of 2FPC is made of 40 sources, while the number of MSPs in the ATNF catalog with measured distance is 128. Hence, the renormalization factor we used is $128/40 = 3.2$. The r and z number distributions of *Fermi*-LAT sources are shown in Figure 5, together with the data and the best-fit functions derived from the ATNF catalog sample of sources. The radial distribution of MSPs in the 2FPC catalog follows the radio one, despite of the poor statistics, showing again a peak at the Earth distance from the galactic center. The vertical height distribution dN/dz is well compatible with radio observations far from the galactic plane, while it is observationally biased at very low

Table 2
Relevant Parameters of the *Fermi*-LAT Detected MSPs in the 2FPC

PSR	$l(^\circ)$	$b(^\circ)$	F_γ (10^{-8} ph cm^{-2} s^{-1})	Γ	$E_{\rm cut}$ (GeV)
J0023+0923	111.15	−53.22	1.2 ± 0.4	1.4 ± 0.4	1.4 ± 0.6
J0030+0451	113.14	−57.61	6.6 ± 0.3	1.2 ± 0.1	1.8 ± 0.2
J0034−0534	111.49	−68.07	2.2 ± 0.3	1.4 ± 0.2	1.8 ± 0.4
J0101−6422	301.19	−52.72	0.75 ± 0.14	0.7 ± 0.3	1.5 ± 0.4
J0102+4839	124.93	−14.83	1.3 ± 0.3	1.4 ± 0.3	3.2 ± 1.1
J0218+4232	139.51	−17.53	7.7 ± 0.7	2.0 ± 0.1	4.6 ± 1.2
J0340+4130	154.04	−11.47	1.5 ± 0.2	1.1 ± 0.2	2.6 ± 0.6
J0437−4715	253.39	−41.96	2.7 ± 0.3	1.4 ± 0.2	1.1 ± 0.3
J0610−2100	227.75	−18.18	0.78 ± 0.25	1.2 ± 0.4	1.6 ± 0.8
J0613−0200	210.41	−9.30	2.7 ± 0.4	1.2 ± 0.2	2.5 ± 0.5
J0614−3329	240.50	−21.83	8.5 ± 0.3	1.3 ± 0.1	3.9 ± 0.3
J0751+1807	202.73	21.09	1.1 ± 0.2	1.1 ± 0.2	2.6 ± 0.7
J1024−0719	251.70	40.52	0.2 ± 0.2	...	...
J1124−3653	283.74	23.59	0.94 ± 0.23	1.1 ± 0.3	2.5 ± 0.7
J1125−5825	291.89	2.60	1.1 ± 0.5	1.7 ± 0.2	4.8 ± 2.4
J1231−1411	295.53	48.39	9.2 ± 0.4	1.2 ± 0.1	2.7 ± 0.2
J1446−4701	322.50	11.43	0.73 ± 0.31	1.4 ± 0.4	3.0 ± 1.7
J1514−4946	325.22	6.84	4.1 ± 0.6	1.5 ± 0.1	5.3 ± 1.1
J1600−3053	344.09	16.45	0.22 ± 0.16	0.40 ± 0.47	2.0 ± 0.7
J1614−2230	352.64	20.19	2.0 ± 0.4	0.96 ± 0.22	1.9 ± 0.4
J1658−5324	334.87	−6.63	5.7 ± 0.7	1.8 ± 0.2	1.4 ± 0.4
J1713+0747	28.75	25.22	1.3 ± 0.4	1.6 ± 0.3	2.7 ± 1.2
J1741+1351	37.90	21.62	0.12 ± 0.04	...	...
J1744−1134	14.79	9.18	4.6 ± 0.7	1.3 ± 0.2	1.2 ± 0.3
J1747−4036	350.19	−6.35	1.5 ± 0.7	1.9 ± 0.3	5.4 ± 3.3
J1810+1744	43.87	16.64	4.2 ± 0.5	1.9 ± 0.2	3.2 ± 1.1
J1823−3021A	2.79	−7.91	1.5 ± 0.4	1.6 ± 0.2	2.5 ± 0.6
J1858−2216	13.55	−11.45	0.55 ± 0.28	0.84 ± 0.74	1.7 ± 1.1
J1902−5105	345.59	−22.40	3.1 ± 0.4	1.7 ± 0.2	3.4 ± 1.1
J1939+2134	57.51	−0.29	1.5 ± 0.8	...	...
J1959+2048	59.20	−4.70	2.4 ± 0.5	1.4 ± 0.3	1.4 ± 0.4
J2017+0603	48.62	−16.03	2.0 ± 0.3	1.0 ± 0.2	3.4 ± 0.6
J2043+1711	61.92	−15.31	2.7 ± 0.3	1.4 ± 0.1	3.3 ± 0.7
J2047+1053	57.06	−19.67	0.83 ± 0.36	1.5 ± 0.5	2.0 ± 1.1
J2051−0827	39.19	−30.41	0.24 ± 0.13	0.50 ± 0.76	1.3 ± 0.7
J2124−3358	10.93	−45.44	2.7 ± 0.3	3.68 ± 0.16	1.63 ± 0.19
J2214+3000	86.86	−21.67	3.0 ± 0.3	1.2 ± 0.1	2.2 ± 0.3
J2215+5135	99.46	−4.60	1.0 ± 0.3	1.3 ± 0.3	3.4 ± 1.0
J2241−5236	337.46	−54.93	3.0 ± 0.3	1.3 ± 0.1	3.0 ± 0.5
J2302+4442	103.40	−14.00	2.6 ± 0.3	0.94 ± 0.12	2.1 ± 0.3

Notes. Column 1: pulsar name; Columns 2 and 3: galacto-centric longitude and latitude; Column 4: photon flux in the 0.1–100 GeV energy band, F_γ. Columns 5 and 6: spectral index Γ and cutoff energy $E_{\rm cut}$.

distances, showing a flattening mainly due to the *Fermi*-LAT sensitivity suppression, as shown in Section 5.1.

We assume the intrinsic dN/dz distribution of MSPs in the Galaxy to be the one deduced from the ATNF sample (see Equation (8)). We show in Section 5.1 that the convolution of the ATNF distribution with the *Fermi*-LAT sensitivity gives a dN/dz compatible with that observed for the *Fermi*-LAT MSPs.

4. MONTE CARLO SIMULATION OF THE γ-RAY GALACTIC MSP POPULATION

The sample of Table 2 is too poor to derive the γ-ray luminosity function directly from γ-ray data, as has been possible, for example, for blazars, (Di Mauro et al. 2014b; Ajello et al. 2014, 2012). On the other hand, it is not even possible to rely on some correlation between γ-ray luminosity and luminosities in other wavelengths (e.g., radio one), due to the high uncertainty on the γ-ray production mechanisms in MSPs, as has been done for misaligned AGNs (Di Mauro et al. 2014a) and star-forming galaxies (Ackermann et al. 2012b). Therefore, since we are able to describe the space, period, and magnetic field distributions of galactic MSPs, we build an MC simulation of the MSP population in order to analyze the properties of this source class in γ ray. We can use the general properties of the MSP population to construct a mock set of sources and find the ensuing γ-ray diffuse emission. This approach has been used, e.g., in Siegal-Gaskins et al. (2011); Grégoire & Knödlseder (2013).

An MSP population is generated according to the P, B, r, and z distributions discussed in Section 2 and 3. The position of each simulated source is assigned by randomly drawing pairs of r, z from the spatial distribution (derived from Equations (8) and (13):

$$\frac{d^2N}{drdz} \propto \exp\left(-\frac{r^2}{2\sigma_r^2} - \frac{|z|}{z_0}\right) \tag{17}$$

with $\sigma_r = 10$ kpc and $z_0 = 0.67$ kpc. We normalize it as a probability distribution function. The same holds for the normalization of every other distribution assumed here.

4.1. The γ-Ray Luminosity Relation with the Spin-down Luminosity

As for the modeling of the γ-ray emission, we assume that the energy loss $\dot{E}$, Equation (2), due to the magnetic-dipole braking is converted into γ radiation. We therefore extract a value for the spin period P and the magnetic field B from the distributions in Equations (7) and (5) (with best-fit parameters as in Table 1), and derive the corresponding loss energy rate $\dot{E}$ for each simulated source from Equation (2). The conversion of $\dot{E}$ into γ-ray luminosity is parameterized by an empirical relationship (Siegal-Gaskins et al. 2011; Grégoire & Knödlseder 2013; Faucher-Giguère & Loeb 2010):

$$L_\gamma = \eta \dot{E}^\alpha, \tag{18}$$

where L_γ and $\dot{E}$ are in units of erg s^{-1}, and η is the conversion efficiency of spin-down luminosity into γ-ray luminosity, hereafter called conversion efficiency. Equation (18) is an effective way to model the MSP γ-ray emission and represents a general expression of the correlation between these two quantities that is often used in the literature. α has usually been empirically chosen to be 0.5 (Faucher-Giguère & Loeb 2010; Siegal-Gaskins et al. 2011) or 1.0 (Grégoire & Knödlseder 2013), although the former value α might be 0.5 theoretically motivated in the framework of the outer gap models of high-energy γ-ray emission. We display in Figure 6 the values of L_γ and $\dot{E}$ for the 40 MSPs of the 2FPC catalog. Horizontal error bars are associated with the uncertainties on the measured period P and $\dot{P}$ (see Equation (2)), while vertical error bars are derived by propagating the uncertainties on the γ-ray parameters Γ, the normalization of the spectrum dN/dE, the energy cutoff $E_{\rm cut}$, and the measured distance of the source. The criticality of the relation Equation (18) $L_\gamma(\dot{E})$ is visible by the scatter of the data points in Figure 6. This scatter prevents us from finding a statistically meaningful relation $L_\gamma(\dot{E})$. In order to probe Equation (18) by means of further γ-ray information, we derive 95% C.L. upper limits (ULs) on the γ-ray flux of a sample of 19 sources non-detected by the *Fermi*-LAT. Those sources were selected in the ATNF catalog as those expected to be the most powerful γ-ray emitters if standard values of $\alpha = 1$ and $\eta = 0.1$ are assumed. We select only sources with latitudes $|b| \geqslant 10^\circ$ in order to avoid

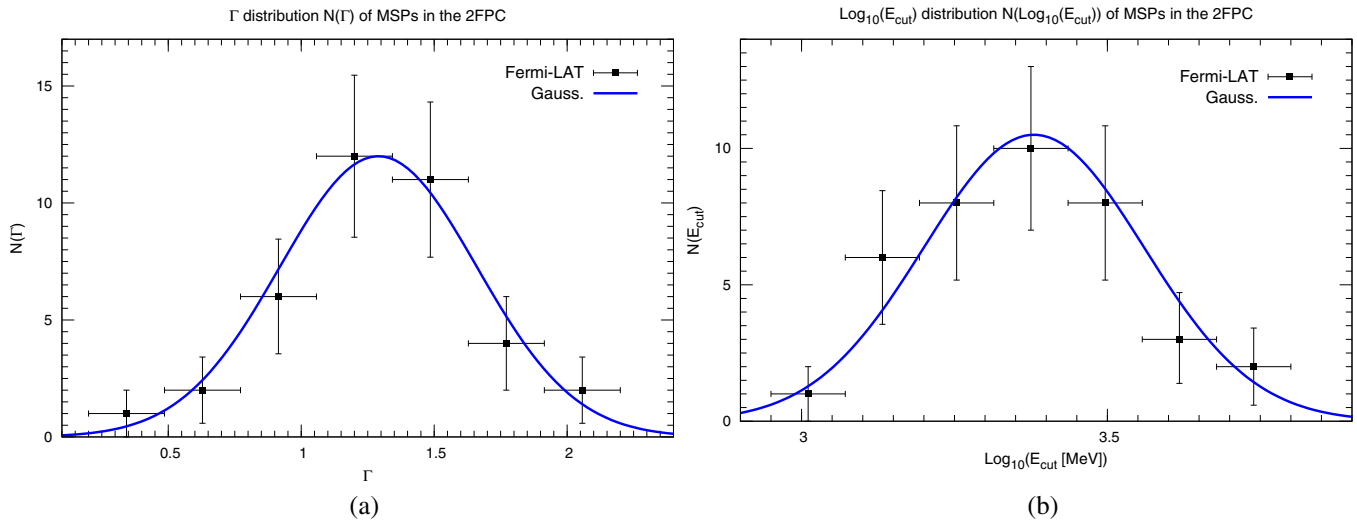

Figure 4. Distribution of spectral index Γ (left panel) and cutoff energy $E_{\rm cut}$ (right panel) of *Fermi*-LAT MSPs in Table 2. The solid blue line refers to the fit with a Gaussian function with best-fit parameters $[\Gamma, \sigma_\Gamma] = [1.29, 0.37]$ and $[\tilde{E}_{\rm cut}, \sigma_{\tilde{E}_{\rm cut}}] = [3.38, 0.18]$, respectively.
(A color version of this figure is available in the online journal.)

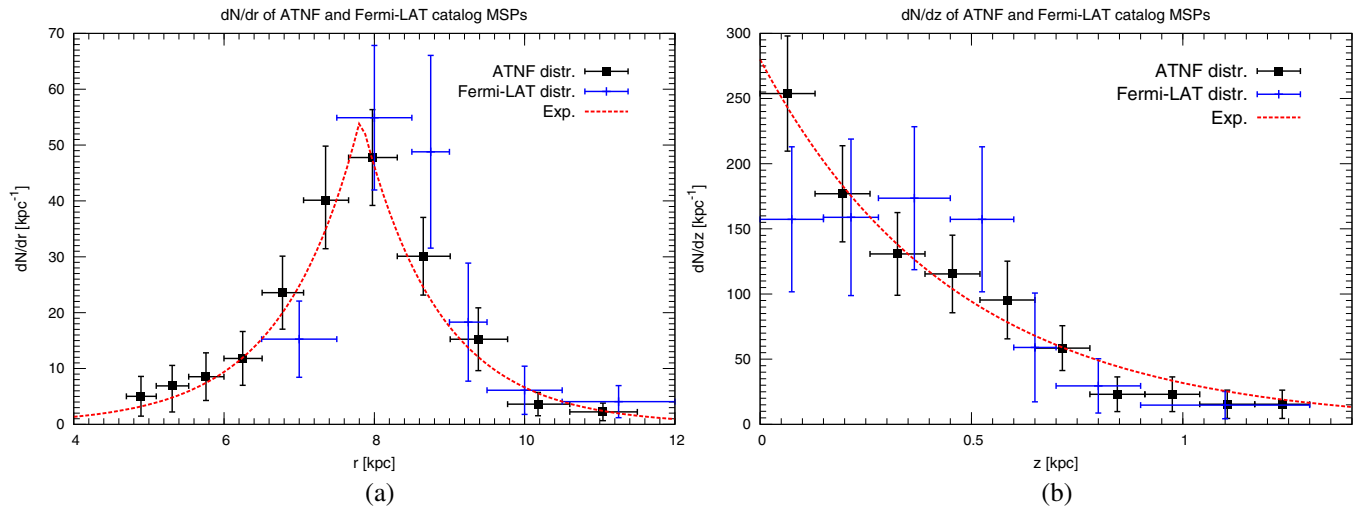

Figure 5. Distribution of radial distance r (left panel) and height from the galactic plane z (right panel) of MSPs in the γ-ray 2FPC (Table 2) is represented by the blue data points, while black points and the dashed red line refer to the distribution and best fit of MSPs in the ATNF radio catalog.
(A color version of this figure is available in the online journal.)

the strong contamination from the galactic foreground. For this purpose we use the *Fermi*-LAT Science Tools.[6]

We choose for the analysis the same data taking period of the 2FPC catalog—from 2008 August 4 to 2011 August 4. The Mission Elapsed Time (MET) interval runs from 239557414 to 334713602. Data are extracted from a region of interest (ROI) of radius = 10° centered at the position of the source, where we select the γ rays in the energy range 100 MeV–100 GeV. We use the P7REP_SOURCE_V15 Event Selection model, take into account the common cut of the rocking angle (selected to be less than 52°), and apply a cut on the zenith angle of 100°. A binned maximum-likelihood analysis is performed. Upper limits of the MSP γ-ray flux are derived by the aid of the LATAnalysisScripts[7], which make use of the UpperLimits.py module. The MSP source spectrum is modeled by a power-law with an exponential cutoff as in Equation (14). $E_{\rm cut}$, Γ, and the flux normalization are considered to be free parameters. Besides the spectral parameters for the sources of the 2FGL catalog close to the investigated source (inside 13° about the source position), additional free parameters are the normalizations of the diffuse backgrounds, namely the galactic diffuse emission (gll_iem_v05.fits) and the isotropic background (iso_source_v05.txt). The 95% C.L. ULs are computed with a profile likelihood method for the 19 sources because no evidence of detection is found (the Test Statistic (TS) is less than 25 for all sources). The 95% C.L. ULs on the integrated flux in the energy range 100 MeV–100 GeV are listed in Table 3. We have taken the values of the longitude l, the latitude b, the distance d from the ATNF catalog, and the spin-down luminosity $\dot{E}$ as derived from measurements according to Equation (2). Given the ULs on F_γ, we then derived the ULs on the γ-ray luminosity using Equation (19), fixing Γ and $E_{\rm cut}$ to the average values derived in Section 3.

We display in Figure 6 the ULs of the γ-ray luminosities. Taking into account the MSPs of the 2FPC catalog and the derived ULs of the sample in Table 3, we identify a benchmark

[6] http://fermi.gsfc.nasa.gov/ssc/data/analysis/documentation. Software version v9r32p5, Instrumental Response Functions (IRFs) P7_V15
[7] User contributions http://fermi.gsfc.nasa.gov/ssc/data/analysis/user/.

Table 3
95% C.L. ULs on the γ-Ray Integrated Photon Flux and Luminosity

PSR	$l(^\circ)$	$b(^\circ)$	d(kpc)	$\dot{E}(\mathrm{s}^{-1})$	$F_\gamma^{UL}(\mathrm{ph\,cm^{-2}\,s^{-1}})$	$L_\gamma^{UL}(\mathrm{erg\,s^{-1}})$
J0218+4232	139.51	−17.53	2.64	$2.4 \times 10^{+35}$	4.55×10^{-08}	$3.94 \times 10^{+34}$
J0514-4002A	244.51	−35.04	12.6	$3.7 \times 10^{+32}$	6.07×10^{-09}	$1.20 \times 10^{+35}$
J1017-7156	291.56	−12.55	3.00	$8.0 \times 10^{+33}$	1.03×10^{-08}	$1.15 \times 10^{+34}$
J1023+0038	243.49	45.78	1.37	$9.8 \times 10^{+34}$	2.42×10^{-08}	$5.65 \times 10^{+33}$
J1300+1240	311.31	75.41	0.62	$1.9 \times 10^{+34}$	3.37×10^{-08}	$2.12 \times 10^{+34}$
J1327-0755	318.38	53.85	1.70	$3.6 \times 10^{+34}$	9.02×10^{-09}	$3.24 \times 10^{+33}$
J1342+2822B	42.22	78.71	10.40	$5.4 \times 10^{+34}$	8.52×10^{-09}	$1.15 \times 10^{+35}$
J1455-3330	330.72	22.56	0.75	$1.9 \times 10^{+33}$	9.65×10^{-09}	$1.61 \times 10^{+33}$
J1544+4937	79.17	50.17	2.20	$1.2 \times 10^{+34}$	2.86×10^{-08}	$5.12 \times 10^{+33}$
J1623-2631	350.98	15.96	2.20	$1.9 \times 10^{+34}$	3.53×10^{-08}	$1.61 \times 10^{+33}$
J1709+2313	44.52	32.21	1.83	$1.4 \times 10^{+33}$	5.74×10^{-09}	$2.39 \times 10^{+33}$
J1740-5340A	338.16	−11.97	3.20	$1.4 \times 10^{+35}$	1.05×10^{-08}	$1.33 \times 10^{+34}$
J1909-3744	359.73	−19.60	0.46	$2.2 \times 10^{+34}$	4.92×10^{-09}	$1.23 \times 10^{+33}$
J1933-6211	334.43	−28.63	0.63	$3.3 \times 10^{+33}$	2.34×10^{-08}	$1.16 \times 10^{+33}$
J2010-1323	29.45	−23.54	1.29	$1.3 \times 10^{+33}$	1.73×10^{-08}	$3.58 \times 10^{+33}$
J2129+1210E	65.01	−27.31	10.0	$7.0 \times 10^{+34}$	1.46×10^{-08}	$1.82 \times 10^{+35}$
J2129-5721	338.01	−43.57	0.40	$1.6 \times 10^{+34}$	6.16×10^{-09}	$1.23 \times 10^{+33}$
J2229+2643	87.69	−26.28	1.43	$2.2 \times 10^{+33}$	1.27×10^{-08}	$3.23 \times 10^{+33}$
J2236-5527	334.17	−52.72	2.03	$1.1 \times 10^{+33}$	6.77×10^{-09}	$4.67 \times 10^{+33}$

Notes. Column 1: pulsar name; Columns 2 and 3: galacto-centric longitude and latitude; Column 4: distance; Column 5: spin-down luminosity; Column 6: 95% C.L. UL photon flux in the 0.1 to 100 GeV energy band; Column 7: derived 95% C.L. UL γ-ray luminosity.

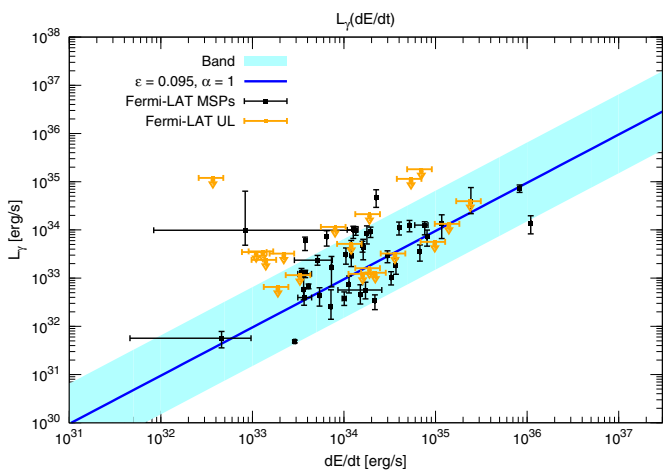

Figure 6. $L_\gamma - \dot{E}$ relation of the *Fermi*-LAT detected sources in the 2FPC (black points), together with the ULs on γ-ray luminosity (orange points) derived from the 95% C.L. ULs on the γ-ray flux for the sources listed in Table 3. The light blue band represents a reasonable range of uncertainty for the $L_\gamma(\dot{E})$ correlation and the average value is drawn (blue solid line) fixing the parameters $\alpha = 1$ and $\eta = 0.095$.

(A color version of this figure is available in the online journal.)

relation with $\alpha = 1$ and $\eta = 0.095$, and an uncertainty band defined by $\eta = \{0.015, 0.65\}$ around $\alpha = 1$. This assumption is based on the scatter in the $L_\gamma - \dot{E}$ plane when considering the 2FPC sources and the derived ULs. We built the band in such a way that almost all the data were within it. We thus stress that it does not correspond to any statistical uncertainty on the correlation, but it is a reasonable way to describe it. Nevertheless, such a scatter represents a fundamental systematic uncertainty that cannot be neglected by simply fixing α and η a priori to single values. We study the uncertainty brought by our ignorance on the real relation $L_\gamma(\dot{E})$ in Section 5 and in the Appendix.

4.2. The γ-Ray Diffuse Emission

The simulated sources are characterized by randomly drawn positions in the Galaxy (r, z), as well as by P and B values extracted from the corresponding distributions. With the latter two quantities, it is possible to derive the energy loss rate $\dot{E}$, Equation (2), and then the γ-ray luminosity, Equation (18). For each source we then compute the energetic flux as:

$$S_\gamma = L_\gamma/(4\pi d^2), \tag{19}$$

where S_γ is defined in the range 0.1–100 GeV, according to Equation (15) in Abdo et al. (2013). By computing the energetic flux from Equation (19) for all simulated sources, we derive the γ-ray flux in the same energy range, F_γ, by assuming that the single source spectral distribution dN/dE is expressed by Equation (14). Spectral index Γ and energy cutoff $E_{\rm cut}$ are drawn from the distributions of Equations (15) and (16) for each source. From the definitions (Abdo et al. 2013):

$$S_\gamma \equiv \int_{E_1}^{E_2} \frac{dN}{dE}\, E\, dE \quad \text{and} \quad F_\gamma \equiv \int_{E_1}^{E_2} \frac{dN}{dE} dE, \tag{20}$$

where $E_1 = 0.1$ GeV, $E_2 = 100$ GeV, $E_0 = 1$ GeV, we can write F_γ as a function of S_γ, Γ, and $E_{\rm cut}$ as:

$$F_\gamma = \frac{S_\gamma}{E_0} \frac{\left[\left(\frac{E_1}{E_0}\right)^{1-\Gamma} \mathcal{E}_\Gamma\left(\frac{E_1}{E_c}\right) - \left(\frac{E_2}{E_0}\right)^{1-\Gamma} \mathcal{E}_\Gamma\left(\frac{E_2}{E_c}\right)\right]}{\left[\left(\frac{E_1}{E_0}\right)^{2-\Gamma} \mathcal{E}_{\Gamma-1}\left(\frac{E_1}{E_c}\right) - \left(\frac{E_2}{E_0}\right)^{2-\Gamma} \mathcal{E}_{\Gamma-1}\left(\frac{E_2}{E_c}\right)\right]}, \tag{21}$$

where $\mathcal{E}_n(t)$ is the exponential integral function arising from the dN/dE integration.

We then classify sources in "non-detected" and "detected" objects. In order to discriminate if the simulated source would have been seen by the LAT or not, we compare its S_γ value with the *Fermi*-LAT detection sensitivity curve $S_t(b)$ displayed

in Figure 17 of Abdo et al. (2013). The LAT sensitivity depends on the position of the source in the Galaxy; e.g., at $|b| = 30^\circ$ it is about 3.2×10^{-12} erg cm^{-2} s^{-1}, while at $|b| = 5^\circ$ it is about 7×10^{-12} erg cm^{-2} s^{-1}. MSPs that have an S_γ above the sensitivity curve are classified as detected. We simulate sources until detected objects reach the number of *Fermi*-LAT observed MSPs above $|b| = 2^\circ$ (i.e., 39). In general, we simulate about 1000–1500 sources, out of which ∼60–100 unresolved objects are found at $|b| \geqslant 10^\circ$.

For the set of non-detected (i.e., unresolved), sources simulated by our MC procedure, we compute the total γ-ray flux in the energy range 0.1–100 GeV as:

$$I_{\rm MSP} = \frac{1}{\Delta\Omega} \sum_{|b| \geqslant b_{\rm min}} F_\gamma, \tag{22}$$

where the sum is made over all the sources with $|b| \geqslant b_{\rm min}$, $\Delta\Omega$ is the solid angle corresponding to $|b| \geqslant b_{\rm min}$, with $b_{\rm min} = 10^\circ$, and F_γ is the γ-ray flux for each source, Equation (21). $I_{\rm MSP}$ represents the unresolved contribution of the simulated MSP population to the IDGRB.

Moreover, by knowing the photon index F_γ, the spectral energy distribution of the single sources, we can get with Equation (20) the spectrum of the total dN/dE by adding up all source contributions at a given energy, and we can draw the total spectrum of the unresolved population of MSPs:

$$\left(\frac{dN}{dE}(E)\right)_{\rm MSP} = \frac{1}{\Delta\Omega} \sum_{|b| \geqslant b_{\rm min}} \frac{dN}{dE}(E). \tag{23}$$

4.3. The γ-Ray Anisotropy

A general prediction (e.g., Siegal-Gaskins et al. 2011) is that a population of γ-ray sources contributes to the γ-ray anisotropy. The *Fermi*-LAT Collaboration has measured the anisotropy of the IDGRB for latitude $|b| > 30^\circ$ in four energy bins spanning from 1 to 50 GeV, namely 1–2 GeV, 2–5 GeV, 5–10 GeV, and 10–50 GeV (Ackermann et al. 2012a). At multipoles $l \geqslant 155$ an angular power above the photon noise level is detected at >99% C.L. in all four energy bins, with approximately the same value $C_P/\langle I\rangle^2 = 9.05 \pm 0.84 \times 10^{-6}$ sr, where $\langle I\rangle$ indicates the average integrated intensity in a given energy range. This result suggests that the anisotropy might originate from the contribution of one or more point-like source populations.

We derive the anisotropy arising from the unresolved MSPs and compare this value with the *Fermi*-LAT data. The angular power C_p produced in the energy range $E \in [E'_1, E'_2]$ by the unresolved flux of γ-ray emitting MSPs is derived using the following equation (Cuoco et al. 2012; Ackermann et al. 2012a):

$$C_p(E'_1 \leqslant E \leqslant E'_2) = \int_{E_{\rm cut,min}}^{E_{\rm cut,max}} dE_{\rm cut} \int_{\Gamma_{\rm max}}^{\Gamma_{\rm min}} d\Gamma \cdot \cdot \int_0^{F'_t(S_t,\Gamma,E_{\rm cut},E'_1,E'_2)} F'^2_\gamma \frac{d^2N}{dF'_\gamma d\Gamma dE_{\rm cut}} dF'_\gamma, \tag{24}$$

where F'_γ is the photon flux of the source integrated in the range $E'_1 \leqslant E \leqslant E'_2$ in units of ph cm^{-2} s^{-1}. $E_{\rm cut}$, min and $E_{\rm cut}$, max are fixed, respectively, to 2.0 and 4.6, while $\Gamma_{\rm min}$ and $\Gamma_{\rm max}$ are fixed to 0.1 and 2.5, respectively. The results do not depend on a slight modification of the limits of integration because these variables are parameterized with Gaussian distributions (see Equations (15) and (16)). F'_t is the flux sensitivity threshold that separates the *Fermi*-LAT detected and undetected MSPs. This quantity depends on the threshold energy flux S_t of the sensitivity map given in the 2FPC catalog. S_t is defined in units of the energy flux integrated in the range 0.1–100 GeV. We choose for S_t a fixed value independent on the latitude. This assumption is justified by the fact that the anisotropy data are valid for $|b| > 30^\circ$, where the LAT sensitivity varies at most by 20% around its average, 3.2×10^{-12} erg cm^{-2} s^{-1}. Therefore, we fix $S_t = 3.2 \times 10^{-12}$ erg cm^{-2} s^{-1}. This flux is integrated in the range 0.1–100 GeV, but the measured C_P are given in another energy range $E'_1 \leqslant E \leqslant E'_2$. Hence, given the photon index Γ and the energy cutoff $E_{\rm cut}$ in the F'_γ integration of Equation (24), we can find the flux threshold F'_t in the C_P energy range $E'_1 \leqslant E \leqslant E'_2$ by taking into account the relation between the photon flux F'_γ and the energy flux S_γ (see Equation (20)) in the range $E_1 \leqslant E \leqslant E_2$:

$$F'_t(S_t, \Gamma, E_{\rm cut}, E'_1, E'_2) = \frac{S_t}{\int_{E_1}^{E_2} E(\frac{E}{E_0})^{-\Gamma} \exp\left(-\frac{E}{E_{\rm cut}}\right) dE} \cdot \cdot \int_{E'_1}^{E'_2} \left(\frac{E}{E_0}\right)^{-\Gamma} \exp\left(-\frac{E}{E_{\rm cut}}\right) dE. \tag{25}$$

In Equation (24), $d^3N/(dF'_\gamma d\Gamma dE_{\rm cut})$ is the differential distribution with respect to the flux, photon index, and energy cutoff, and is usually factorized by three independent functions (Cuoco et al. 2012; Ackermann et al. 2012a):

$$\frac{d^3N}{dF'_\gamma d\Gamma dE_{\rm cut}} = \frac{dN}{dF'_\gamma}\frac{dN}{d\Gamma}\frac{dN}{dE_{\rm cut}}, \tag{26}$$

where $dN/d\Gamma$ and $dN/dE_{\rm cut}$ are given by Gaussian distributions as in Section 3. dN/dF'_γ is usually (see, e.g., Cuoco et al. 2012; Ackermann et al. 2012a; Abdo et al. 2010a) described by a broken power law:

$$\frac{dN}{dF'_\gamma} = \begin{cases} A F'^{-\beta}_\gamma & F'_\gamma \geqslant F_b \\ A F'^{-\alpha}_\gamma F_b^{\alpha-\beta} & F'_\gamma < F_b \end{cases}, \tag{27}$$

where A is a normalization factor in units of cm^2 s^{-1} sr^{-1}, F_b is the break flux, and α and β are the slopes of dN/dF'_γ below and above the break, respectively. As shown in Section 5.3, the broken power law is adequate to parameterize the flux distribution of MSPs.

In order to find the values of A, β, α, and F_b, we fit the MC MSP flux distribution with the theoretical flux distribution given by the following equation:

$$\frac{dN}{dF'_{\gamma\ \rm fit}} = \int_{E_{\rm cut,min}}^{E_{\rm cut,max}} \int_{\Gamma_{\rm min}}^{\Gamma_{\rm max}} \frac{dN}{dF'_\gamma d\Gamma dE_{\rm cut}} d\Gamma dE_{\rm cut}. \tag{28}$$

5. RESULTS

5.1. Contribution to the High-latitude γ-Ray Diffuse Background

By following the MC procedure highlighted in Section 4, we generate a MSP population that follows the assumed distributions in period, magnetic field, and distance; the γ-ray spectral properties of the simulated sources reflect the distributions of observed γ-ray MSPs (Equations (15)–(16)).

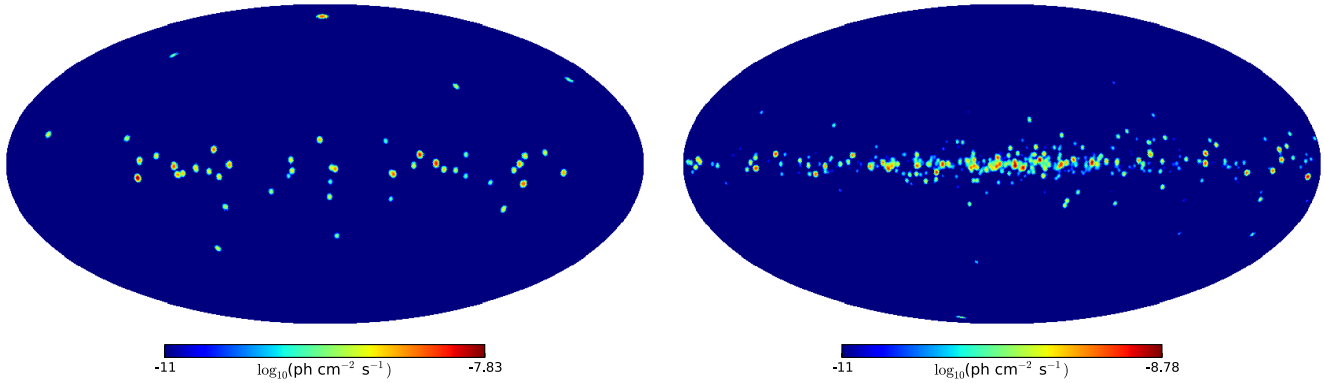

(a) (b)

Figure 7. All-sky γ-ray map of the MC simulated MSP population for the best fit realization. The left panel shows the sources that would be detected by the LAT, while the unresolved counterpart is displayed in the right panel. The different color scale is chosen to allow a better visual effect and a smoothing of $1\overset{\circ}{.}5$ is applied to the maps.

(A color version of this figure is available in the online journal.)

To account for the uncertainty due to the conversion of the spin-down luminosity into the γ-ray luminosity for each simulated source, we extract the conversion efficiency η (Equation (18)) from a $\log_{10}$ uniform distribution in the range $\log_{10}(0.015)$–$\log_{10}(0.65)$, with mean value 0.095, as represented in Figure 6. Moreover, we parameterize the sensitivity of the LAT to MSP detection using a latitude-dependent function $S_t(b)$ with a normalization that corresponds to the best-fit value of the *Fermi* -LAT sensitivity curve, and with a dispersion given by the 10% and 90% percentile sensitivity (see Figure 17 of Abdo et al. 2013). In the MC procedure, we randomly extract for each source a value for the normalization of the flux sensitivity function $S_t(b)$, bracketing this uncertainty.

As an additional source of uncertainty, we consider the dependence of the prediction on the single MC realization. Taking into account all the above cited distributions (i.e., for the vertical and radial distances), the spin period, surface magnetic field, spectral γ-ray parameters Γ and $E_{\rm cut}$, conversion efficiency η, and normalization of the sensitivity function, we perform 1000 MC realizations of the MSP population in the Galaxy. Our final goal is to compute the average differential energy distribution dN/dE from unresolved MSPs and its uncertainty. The total differential energy spectrum of unresolved MSPs is given by the sum of the single source spectra at any energy (see Equation (23)). Since for each source with spectrum as in Equation (14) we do not assume a universal value for the spectral parameters but rather assign Γ and $E_{\rm cut}$ randomly to each single simulated source from the distributions of Equations (15) and (16), the total differential energy spectral shape may vary slightly from one realization to another. To guarantee a precise reconstruction of the average total spectral distribution in the whole energy range, and taking into account that the spectrum rapidly varies at low energies ($E \lesssim 3$ GeV), we derive the probability distribution function (PDF) of the integrated fluxes (see Equation (22)) above three fixed energy thresholds: 0.1 GeV, 0.7 GeV, and 1.5 GeV. The PDFs are consistent with a Gaussian for all the three energy thresholds, for which we derive mean and dispersion $sigma$ of the corresponding integrated flux distribution. The MC realizations that have integrated fluxes above 0.1 GeV, 0.7 GeV, and 1.5 GeV equal to the mean flux, the mean flux $\pm 1\sigma$ for all the three integrated flux distributions corresponding to the three fixed threshold energies are identified, respectively, as our best fit, $\pm 1\sigma$ configurations. The average prediction on the total diffuse emission is computed from the best-fit configuration, while the uncertainty band is delimited by the $\pm 1\sigma$ realizations. Therefore, the "1σ" of the 1σ uncertainty band is primarily meant to indicate the dispersion on the integrated flux distributions.

A typical γ-ray all-sky map[8] of our simulated population is shown in Figure 7. We chose the best fit realization that gives the best-fit curve for the diffuse γ-ray emission in Figure 9. In order to highlight the properties of the population, we decide to separately display the resolved (left panel) and unresolved (right panel) components. The color scale is chosen to allow the reader to see most of the sources, even when they have very low fluxes. The detected sources are determined by the implementation of the *Fermi*-LAT 2FPC sensitivity, as explained above.

We have already shown that the intrinsic distribution of z, assumed to be the one derived from the ATNF catalog, and the one calculated from the *Fermi*-LAT MSPs are different close to the galactic plane (see Figure 5). We can demonstrate that the reason for this is associated to the *Fermi*-LAT sensitivity flux, which is at least a factor of two larger in the galactic center with respect to high-latitude regions ($|b| \geqslant 10^\circ$). In order to verify this assumption we derived the dN/dz for an MC realization of the MSP population, which represents the theoretical result deduced from the intrinsic ATNF distribution convolved with the *Fermi*-LAT sensitivity. We renormalized the dN/dz in each bin to take into account the different number of sources between the MC and the ATNF catalog. In Figure 8 the dN/dz is shown for the sources in the ATNF, *Fermi*-LAT catalogs and for MC simulated sources. We also display the theoretical best fit for the ATNF catalog MSPs. It is clear that, considering the dN/dz derived from the best fit of the ATNF catalog sources and convolving this intrinsic distribution with the *Fermi*-LAT sensitivity, we obtain a distribution that is compatible with *Fermi*-LAT data. The rescaled sets of data "Renorm. *Fermi* -LAT" and "Renorm. MC," when compared, have a $\chi^2/d.o.f. = 0.67$, indicating the good agreement between the data and MC. Therefore, in the galactic center

[8] The γ-ray intensity maps have been generated with the HEALPix software (Górski et al. 2005).

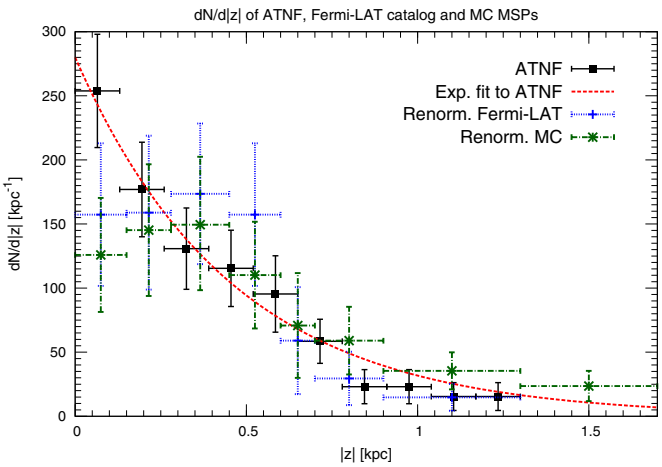

Figure 8. Renormalized distribution of the height z from the galactic plane of *Fermi*-LAT MSPs in Table 2 is represented by the blue dashed data points, while solid black points and dotted line refer to radio distribution and best fit. We also display the renormalized distribution for the detected sources in the MC realization, which gives the best fit of Figure 9 (dot-dashed green points).

(A color version of this figure is available in the online journal.)

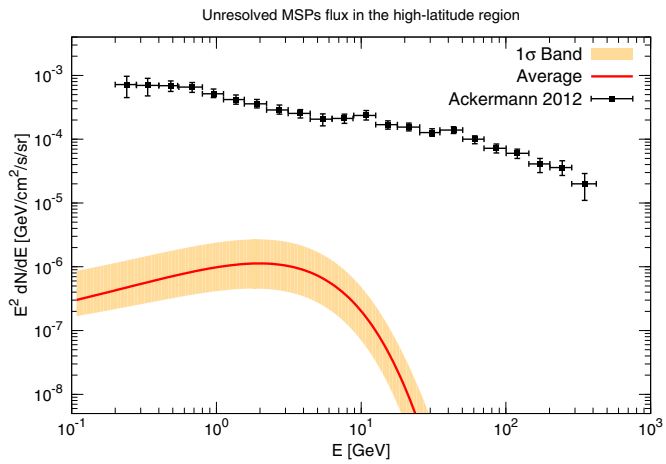

Figure 9. Prediction of the diffuse γ-ray flux at $|b| \geqslant 10^\circ$ from the unresolved population of MSPs as derived from 1000 MC simulations of the MSP galactic population. The red solid line represents the mean spectral distribution (see the text for further details), while the light orange band corresponds to the 1σ uncertainty band. The black points refer to the IDGRB preliminary data taken from Ackermann (2012).

(A color version of this figure is available in the online journal.)

region we do expect a large number of sources, whose detection is prevented from the decreased instrumental sensitivity.

The contribution to the IDGRB at $|b| \geqslant 10^\circ$ from the unresolved MSPs generated by our MC method is shown in Figure 9. The data points refer to the preliminary IDGRB data as taken from Ackermann (2012). The line corresponds to the mean prediction of our 1000 MC realizations, while the band covers the uncertainty due to the choice of the distributions for the vertical and radial distances, spin period, surface magnetic field, spectral γ-ray parameters Γ and $E_{\rm cut}$, η, and normalization of the LAT sensitivity function, and it is derived as explained above.

The MSP total differential energy spectrum in Figure 9 follows a power law with an exponential cutoff, as it is peculiar of the single source spectra of which it is the sum (see Equation (23)). At the peak of the spectral emission, ∼2 GeV, the fraction of the IDGRB due to MSPs is about 0.3% (0.1%, 0.9%) for the best fit (lower, upper) curve; at higher energies the spectrum exponentially decreases, giving almost zero contribution above ∼20 GeV. The MSP spectrum is always more than two orders of magnitude suppressed with respect to the IDGRB data. We notice that the uncertainty is a factor of about five at 0.1 GeV, as well as at 10 GeV.

The integrated intensity in the range 0.1–100 GeV (above $b = 10^\circ$), Equation (22), for the mean curve in Figure 9 is 5.07×10^{-9} ph cm^{-2} s^{-1}sr^{-1}, which corresponds to 0.05% of the IDGRB integrated flux of Abdo et al. (2010b). The upper (lower) edge of the band accounts for 0.13% (0.02%), with an integrated intensity of 1.32×10^{-8} (2.43×10^{-9}) ph cm^{-2} s^{-1} sr^{-1}. We point out that modeling the latitude dependence of the LAT detection sensitivity instead of using a sharp threshold (as usually adopted in previous works) significantly affects the final result. We quantify this discrepancy to be about a factor of two in the differential flux when using a universal threshold of 10^{-8} ph cm^{-2} s^{-1}.

The contribution of unresolved MSPs to the IDGRB is found to be smaller than what previously estimated, e.g., in Siegal-Gaskins et al. (2011); Grégoire & Knödlseder (2013). In Grégoire & Knödlseder (2013), the contribution at $|b| \geqslant 40^\circ$ is estimated to be about 1.5×10^{-8} ph cm^{-2} s^{-1} sr^{-1}, whereas we find 0.6×10^{-9} ph cm^{-2} s^{-1} sr^{-1}. The main difference is caused by the values of the assumed parameters z_0 and $\langle \log_{10}(B/G) \rangle$. Both parameters are, in our model, significantly lower than in Grégoire & Knödlseder (2013), implying a strong depression of the final flux. We have checked explicitly that with $z_0 = 1.8$ kpc and $\langle \log_{10}(B/G) \rangle = 8$ (as in their FG1 reference model that is directly translatable into ours), we get an integrated flux above $b = 40^\circ$ of 1.8×10^{-8} ph cm^{-2} s^{-1} sr^{-1}.

5.2. Contribution of Pulsars to the Inner Galaxy and to the Galactic Center γ-Ray Diffuse Background

As we have already seen in Section 2, MSPs are concentrated along the galactic disk and their number decreases as the latitude grows. Therefore, although it is possible to find about 75% of MSPs in the 2FPC (30 out of a total of 40 sources) at high latitudes ($|b| \geqslant 10^\circ$), we expect a large number of sources in the inner region of the Galaxy. Moreover, at low latitudes close to the disk, the population of young γ-ray pulsars is very abundant. Indeed, despite the sensitivity threshold the number of young pulsars near the galactic center is about a factor of 11 larger than at high latitudes, where only seven out of 77 objects are found in the 2FPC. This implies that the γ-ray emission from unresolved pulsars, both young and millisecond, in the innermost part of the Galaxy might be significant and cover an important fraction of the diffuse emission at low latitudes. In this region of the Galaxy an excess emission in the *Fermi*-LAT γ-ray data, with respect to standard astrophysical foregrounds and backgrounds, has recently been claimed by different groups (Hooper & Slatyer 2013; Gordon & Macias 2013; Abazajian et al. 2014).

We therefore derive the γ-ray flux from the unresolved young pulsars and MSPs in the inner part of our Galaxy by analyzing two different regions of the sky.

In order to model the distribution of young pulsars in the Galaxy and their γ-ray emission we follow the same method explained in Sections 2–4. The ATNF catalog contains about 2000 sources with $P > 15$ ms (Manchester et al. 2005) which, according to the adopted convention, are classified as young pulsars. Those objects have a space distribution similar to that of

Table 4
Best fit Parameters for a $\log_{10}$ Gaussian Distribution for the Magnetic Field B and the Period P, for an Exponential Function for the Distance from the Galactic Plane z and the Radial Distance r, and for a $\log_{10}$ Gaussian Distribution for the Cutoff Energy $E_{\rm cut}$ and a Gaussian for the Photon Index Γ for Our Sample of Young Pulsars Taken from the ATNF Catalog (Manchester et al. 2005) and from the 2FPC (Abdo et al. 2013)

B	$\langle\log_{10}(B/\mathrm{G})\rangle$	$\sigma_{\log_{10} B}$	P	$\langle\log_{10}(P/\mathrm{s})\rangle$	$\sigma_{\log_{10} P}$	$\langle\log_{10}(E_{\rm cut}/\mathrm{MeV})\rangle$	$\sigma_{\log_{10} E_{\rm cut}}$
	12.06 ± 0.06	0.55 ± 0.08		-0.21 ± 0.03	0.38 ± 0.04	3.35 ± 0.09	0.26 ± 0.04
r	$\langle r\rangle$[kpc]	r_0[kpc]	z	$\langle z\rangle$[kpc]	z_0[kpc]	$\langle\Gamma\rangle$	σ_Γ
	6.4 ± 0.2	3.1 ± 0.3		0.00 ± 0.09	0.10 ± 0.05	1.51 ± 0.04	0.32 ± 0.05

MSPs, but are more concentrated toward the galactic center. We study the spatial distribution of young pulsars as we have done for MSPs in Section 2. We deduce that the spatial vertical height distribution dN/dz of sources is well described by an exponential (Equation (8)) with $z_0 = 0.10$ kpc. Such value for z_0 indicates that young pulsars are more concentrated along the galactic plane with respect to MSPs ($z_0 = 0.67$ kpc). The average radial distance of the dN/dr is $\langle r\rangle = 6.5$ kpc and the distribution does not show a clear peak. It has been demonstrated in Lorimer et al. (2006), Faucher-Giguere & Kaspi (2006), and Yusifov & Kucuk (2004) that the intrinsic distribution of young pulsars should peak at about 3–4 kpc from the galactic center because these sources are born in the galactic spiral arms. Following the evolution of this population by starting from its birth distribution could broaden the evolved distribution and move its peak to 6–7 kpc (Faucher-Giguere & Kaspi 2006). Hence, we consider the same radial distribution derived by Yusifov & Kucuk (2004), which is compatible with the model derived in Lorimer et al. (2006). This distribution has a peak at 3.2 ± 0.4 kpc, a scale-length of 3.8 ± 0.4 kpc, and a depletion of the number of sources when moving toward the galactic center:

$$\frac{dN}{dx} \propto x^{\alpha} \exp\left(-\beta\left(\frac{x - x_{\rm sun}}{x_{\rm sun}}\right)\right), \tag{29}$$

with $\alpha = 1.64$, $\beta = 4.01$, $x = r + r_1$, $x_{\rm sun} = r_{\rm sun} + r_1$, and $r_1 = 0.55$. This radial distribution is compatible with the observed distribution of the young pulsars of the ATNF catalog (Manchester et al. 2005) and Parkes catalog (Lorimer et al. 2006).

The surface magnetic field and the rotational period are adequately fitted by a $\log_{10}$ Gaussian distribution (see Equations (7) and (5)) with $\langle\log_{10}(B/\mathrm{G})\rangle = 12.1$, $\sigma_{\log_{10} B} = 0.6$, and $\langle\log_{10}(P/\mathrm{s})\rangle = -0.21$, $\sigma_{\log_{10} P} = 0.38$. The radial distance r, vertical height z, rotational period P, and surface magnetic field distributions we derive for the young pulsars in the ATNF catalog are compatible with those deduced in Lorimer et al. (2006), Faucher-Giguere & Kaspi (2006), Yusifov & Kucuk (2004), and Faucher-Giguère & Loeb (2010).

The γ-ray spectral properties are derived from the sample of 77 young pulsars of the 2FPC. We fit the cutoff energy $E_{\rm cut}$ and the photon index Γ with a logarithmic base 10 and a linear Gaussian distribution, and we find the following best-fit parameters: $\langle\log_{10}(E_{\rm cut}/\mathrm{MeV})\rangle = 3.35$, $\sigma_{\log_{10} E_{\rm cut}} = 0.26$, $\langle\Gamma\rangle = 1.51$ and $\sigma_\Gamma = 0.32$. We show in Table 4 the best-fit values and uncertainties for the parameters of our young pulsar sample.

As for the γ-ray emission, we consider again the relation L_γ and $\dot{E}$ (see Equation (18)), by adapting the parameters α and η to the data for young pulsars. In this case we fix $\alpha = 1$, $\langle\eta\rangle = 0.080$, and $\eta = [0.009, 0.75]$.

By adopting the same method used for MSPs (Sections 4–5.1), we derive the γ-ray emission from the unresolved counterpart of MSP and young pulsar populations in different regions at intermediate and low latitudes. In order to compare with the previous literature we consider: $10^\circ \leqslant |b| \leqslant 20^\circ$ and $l \in [-180^\circ, 180^\circ]$ (i.e., hereafter the inner Galaxy region), and $|b| \leqslant 3.5^\circ$ and $|l| \leqslant 3.5^\circ$ (i.e., hereafter the galactic center region). The result is displayed in Figure 10, where we show the emission from unresolved young pulsars, MSPs, and from their sum.

The left panel refers to the contribution to the inner Galaxy region, where the MSP contribution dominates the pulsars' diffuse γ-ray flux, because at those latitudes only few young pulsars are present. For comparison, the excess emission in the same region derived by Hooper & Slatyer (2013) is shown. Instead, in the galactic center region (right panel of Figure 10) the MSP and young pulsar populations give about the same contribution to the diffuse emission. The overlaid data sets refer to three analyses performed in the galactic center region, which found similar results (Gordon & Macias 2013; Abazajian et al. 2014). The two different results for the excess from Abazajian et al. (2014) are obtained by differently modeling the background and templates for point sources. The discrepancy, in particular, at low energies is emblematic of the great uncertainty in the determination of the excess spectrum. The spectral shape of the young pulsar contribution differs from that of the MSPs because of the different best-fit values of the Γ and $E_{\rm cut}$ distributions. The uncertainty band of young pulsars is, in general, wider with respect to that of MSPs because of the larger uncertainty on the η parameter.

Considering the inner Galaxy region we find that only about 5% of the excess in Hooper & Slatyer (2013) at 1–3 GeV (where the emission peaks) can be covered by the total unresolved pulsars population. This result, although more conservative, is in agreement with the estimate of Hooper et al. (2013) and the differences may be traced back in a slightly higher value of the magnetic field and the detection threshold assumed. In the innermost region of the Galaxy (i.e., the galactic center region) we find that the flux from unresolved pulsars may account for about 8% of the excess emission at the peak ($\sim$1 GeV) derived by Gordon & Macias (2013) and Abazajian et al. (2014) (model I). Additionally, Gordon & Macias (2013) give an interpretation of the excess as due to an unresolved population of pulsars with the spectral energy distribution given by Equation (14) with $\Gamma = 1.6 \pm 0.2$ and $E_{\rm cut} = 4000 \pm 1500$ MeV. To make a comparison with this result, we derive Γ and $E_{\rm cut}$ for the total pulsars emission with the function of Equation (14) (fixing $E_0 = 1176$ MeV as in Gordon & Macias 2013) and find best-fit spectral index Γ and $E_{\rm cut}$ equal to, respectively, -1.53 and 3390 MeV, which are compatible with Gordon & Macias (2013) with, however, a different normalization factor.

Our result is not in contrast with Yuan & Zhang (2014), which could explain the whole excess in terms of MSPs. Indeed, we do not consider here the MSP population from the bulge, but only the one from the disk. Adding a second MSP component,

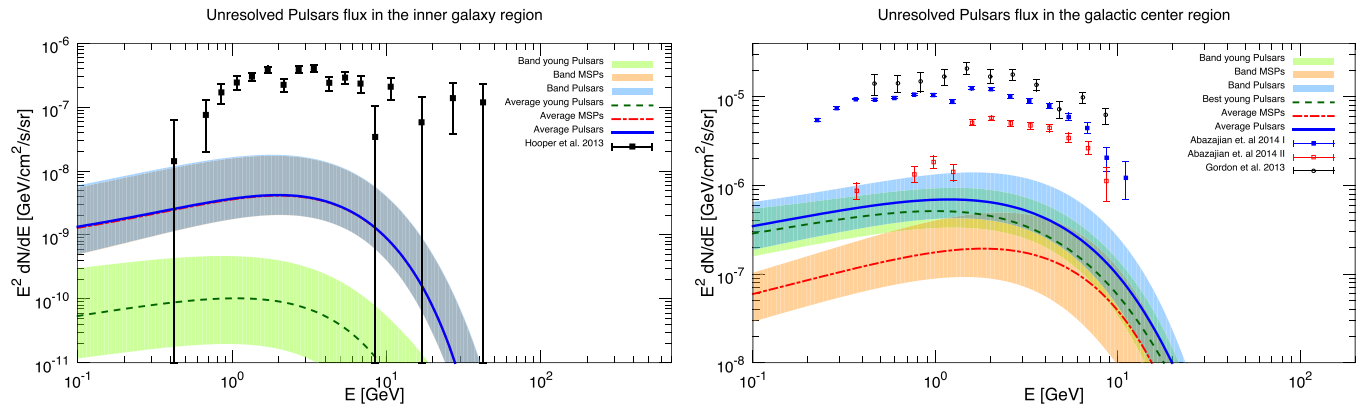

Figure 10. Best fit (band) of the γ-ray flux from the unresolved young pulsars is shown with the dashed green line (green band), from the unresolved MSPs with the dot-dashed red line (orange band), and from the whole pulsars population with the blue solid line (blue band). On the left side, we display the pulsar population contribution in the inner Galaxy region ($10^\circ \leqslant |b| \leqslant 20^\circ$ and $l \in [-180^\circ, 180^\circ]$), while the right panel shows the contribution to the galactic center diffuse emission ($|b| \leqslant 3\overset{\circ}{.}5$ and $|l| \leqslant 3\overset{\circ}{.}5$). The black points in the left panel were taken from Hooper & Slatyer (2013). The black dots in the right panel were taken from Gordon & Macias (2013), whereas the red and blue points correspond to two different analysis carried by Abazajian et al. (2014).

(A color version of this figure is available in the online journal.)

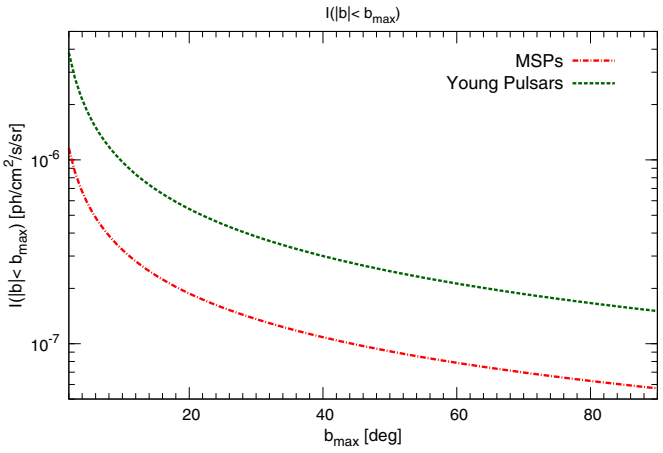

Figure 11. Integrated flux $I(|b| < b_{\max})$ for latitudes smaller than $b_{\max}$, derived with Equation (22) in the energy range 0.1–100 GeV, is shown for MSPs (blue solid line) and young pulsars (red dashed line).

(A color version of this figure is available in the online journal.)

that is, by definition, more concentrated toward the galactic center, would increase the contribution from MSPs at low latitudes. We caution, however, that in those two regions the determination of the excess is very delicate and is a matter of a huge debate because of the great impact of systematics. Future and independent analysis of *Fermi*-LAT data could confirm or refute this result. In particular, the normalization, spectral shape, and morphology of the excess strongly depend on the method used to analyze the data, namely the source catalog, the point source subtraction method, the modeling of the galactic diffuse foreground, and the templates for the different components of the fits.

Finally, in Figure 11, we compare the integrated emission from unresolved MSPs and young pulsars as a function of the latitude, b. The contribution of unresolved pulsars to the IDGRB strongly depends on the latitude, as a consequence of the spatial distribution of the sources. The integrated flux in the energy range 0.1–100 GeV, Equation (22), for different regions of the sky, $|b| < b_{\max}$ is displayed as a function of the maximal latitude $I(|b| < b_{\max})$, with $b_{\max}$ ranging from 2° to 90°. Most of the γ-ray flux coming from the MSPs (young pulsars) is concentrated within 20° (10°) because the most of the emission comes from low latitudes. For high latitudes ($b_{\max} > 20^\circ$) the integrated flux is about one order of magnitude smaller for both populations.

5.3. Contribution of MSPs to the γ-Ray Anisotropy

In this section we present our result on the anisotropy originating from the unresolved MSP population. We follow the method explained in Section 4.3 and derive the 1σ upper limit angular power, C_P. We consider the MC realizations that give best-fit, lower and upper edges of the 1σ uncertainty band of Figure 9 (Section 5.1). For each of these realizations we derive the differential flux distribution $(dN/dF'_\gamma)_{\rm MC}$ of the unresolved MSPs. We divide the range of flux F'_γ in N bins. For each bin $(dN/dF'_\gamma)_{\rm MC}$ is given by the following equation:

$$\left(\frac{dN}{dF'_\gamma}(F'_\gamma \in [F^i_{\rm min}, F^i_{\rm max}])\right)_{\rm MC} = \frac{N^i}{\Delta F'^i_\gamma}, \qquad (30)$$

where $dN/dF'_{\gamma\,\rm MC}$ is calculated in the ith bin defined as $F'_\gamma \in [F^i_{\rm min}, F^i_{\rm max}]$, N^i is the number of unresolved sources in the bin, and $\Delta F^i_\gamma = F^i_{\rm max} - F^i_{\rm min}$ is the width of the bin. $(dN/dF'_\gamma)_{\rm MC}$ represents the differential flux distribution of the unresolved part of the considered MC realization. In Figure 12 we show the result for the realization corresponding to the upper limit of the band in Figure 9. The uncertainties are Poissonian errors, namely $\sqrt{N^i}$, associated to the number of sources in each bin N^i. The realization that gives the lower part of the 1σ uncertainty band of the diffuse γ-ray emission has a too small number of unresolved sources for computing the MC MSP flux distribution, and therefore we are not able to derive the best-fit and 1σ uncertainty values of C_P. Nevertheless, we do compute the 1σ upper limit of C_P considering the realization, which gives the upper bound of the flux band. We calculate the differential distribution $d^3N/(dF'_\gamma d\Gamma dE_{\rm cut})$, defined in Equation (26), performing a fit of the theoretical flux distribution given in Equation (28) with the same quantity derived from the MC realization with Equation (30). In Figure 12 we overlap, for the four energy

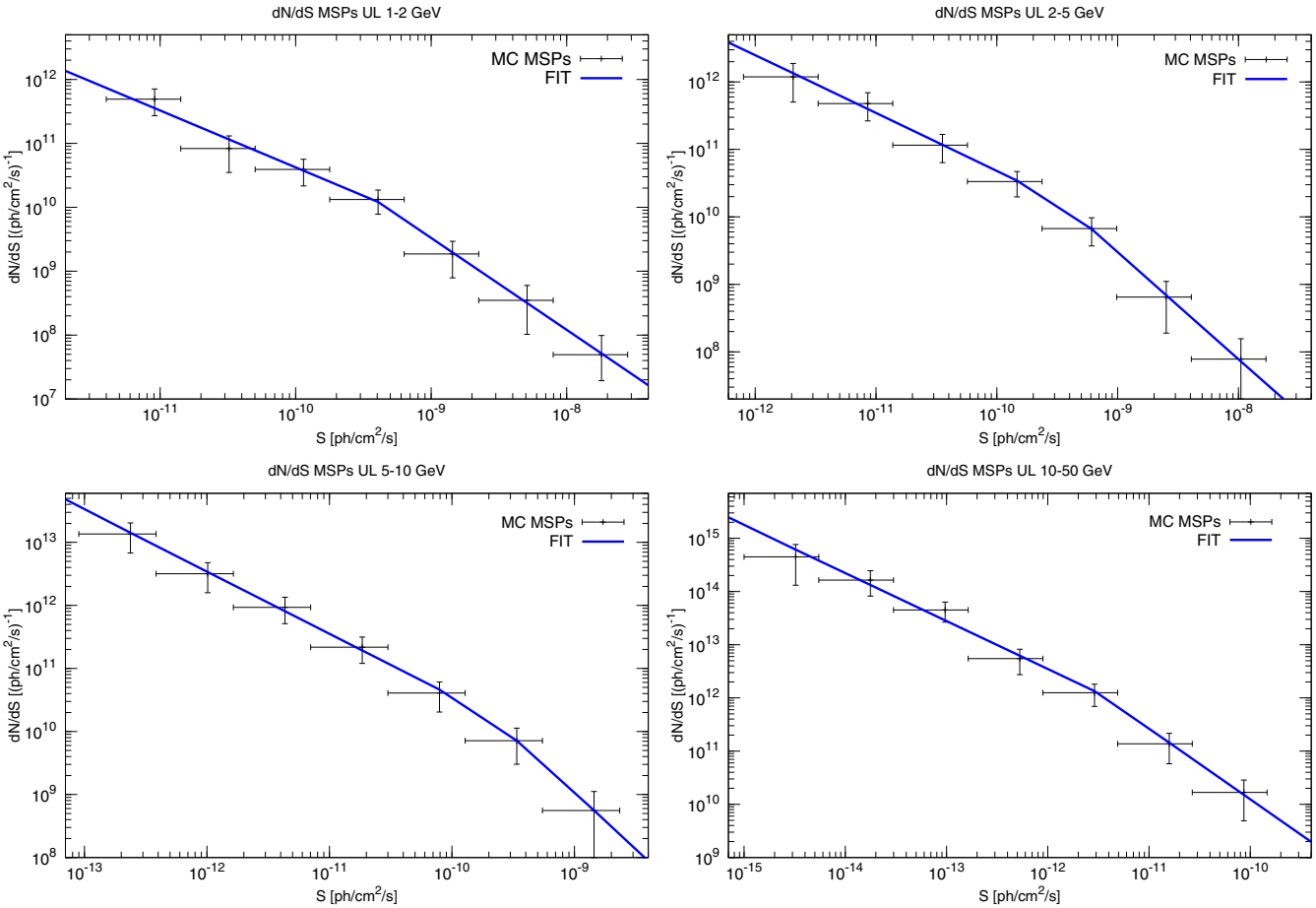

Figure 12. In this figure we display, for the four energy bins quoted in the text, the flux distributions of the MSPs of the + 1σ MC realization (black points) and the best-fit flux distribution derived using Equation (28) (blue solid line).

(A color version of this figure is available in the online journal.)

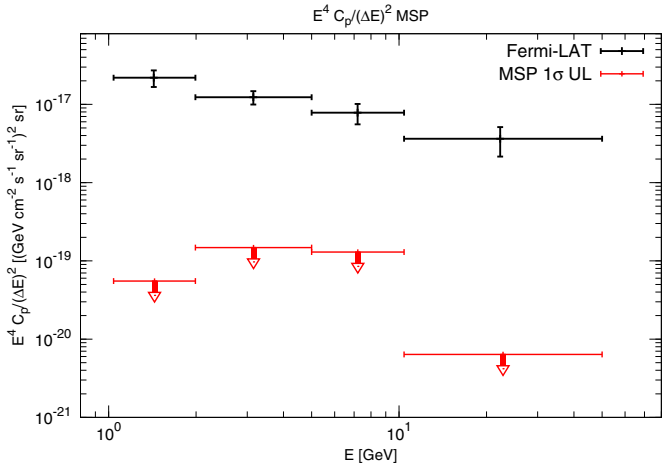

Figure 13. 1σ upper limit angular power C_P from the unresolved MSPs (red points) is shown with *Fermi*-LAT data (Ackermann et al. 2012a; black points).

(A color version of this figure is available in the online journal.)

bins, the flux distribution of the MC realization and the best fit for the theoretical differential distribution.

Taking into account the best-fit distributions $(dN/dF'_\gamma)_{\rm fit}$ derived as described above, we calculate the 1σ upper limit of the angular power C_P using Equation (24). We show the result in Figure 13 together with *Fermi*-LAT results for the DATA:CLEANED event class (Ackermann et al. 2012a). For the sake of completeness, we quote the 1σ upper limit of the angular power C_P in Table 5 for the four energy bins.

The anisotropy from unresolved MSPs is at least a factor of 60 smaller than *Fermi*-LAT data, and therefore MSPs turn out to represent a population that gives a negligible contribution to the *Fermi* -LAT anisotropy. This conclusion is compatible with the expectations of the γ-ray anisotropy produced by radio-loud AGNs and blazars (Cuoco et al. 2012; Di Mauro et al. 2014, in preparation), according to which blazars would dominate the angular power so that any other population should give a negligible anisotropy contribution.

Moreover, we stress that our result represents the first and most up-to-date estimate of anisotropy from MSPs based on γ-ray data. Siegal-Gaskins et al. (2011) was based on the first nine months of *Fermi*-LAT observations of eight MSPs. In particular, at latitudes above 30°, we find that $C_P/\langle I\rangle^2$ is about 0.2 sr in the first energy bin, whereas Siegal-Gaskins et al. (2011) found $C_P/\langle I\rangle^2 \sim 0.03$–$0.04$ at $|b| \geqslant 40°$. The discrepancy of $C_P/\langle I\rangle^2$ is due to different assumptions about the modeling of the γ-ray MSP population, the γ-ray detection sensitivity (assumed there as a fixed threshold), and the region of the sky considered (above $b = 40°$). Such differences imply different values of both the dimension C_P and of the mean average intensity $\langle I\rangle$. We notice that the energy dependence of the MSPs' C_P in Figure 13 is significantly different from the power-law-like behavior of the *Fermi*-LAT data. This strengthens the fact that MSPs cannot be the dominant contributor to the IDGRB anisotropy.

Table 5
The 1σ Upper Limit of the Angular Power C_P in the Four Energy Bins Derived from the Simulation of the MSP Population

Energy Range [GeV]	1.04–1.99	1.99–5.0	5.0–10.4	10.4–50.0
C_P[(cm^{-2} s^{-1} sr^{-1})^2 sr]	1.16×10^{-20}	1.35×10^{-20}	1.40×10^{-21}	3.40×10^{-23}

6. CONCLUSIONS

Motivated by the possibility that MSPs might be an important contributor to the intensity and anisotropy of the IDGRB, we derived the properties of the MSP population in order to build a model consistent with radio and γ-ray observations. Spatial and luminosity distributions have been calibrated on radio observations of 132 sources from the ATNF pulsars catalog. This represents, to our knowledge, the first systematic analysis of such a large MSP sample. The best-fit distributions of the surface magnetic field B, the spin period P, the distance height from the galactic plane z, and the radial distance r have been derived from radio observations.

Spectral and luminosity properties of the γ-ray MSP population were derived from the most up-to-date γ-ray *Fermi*-LAT pulsars catalog, the 2FPC. In particular, we used the information from the 95% C.L. ULs on the γ-ray flux of about 20 MSPs in order to constrain the critical relation $L_\gamma - \dot{E}$ and derive an empirical uncertainty band around the scattered data points.

With the aid of the derived distributions, we were able to simulate the γ-ray MSP population. To do so, we relied on an MC simulation of the MSP distribution in the Galaxy. We ran $\sim$1000 MC simulations to take into account the dispersion on the single MC realization, as well as other main theoretical uncertainties, such as the uncertainty on the coefficient of proportionality of the $L_\gamma - \dot{E}$ relation (i.e., η). By averaging more than 1000 MC realizations, we computed the contribution to the IDGRB at high latitudes due to the unresolved counterpart of the simulated MSP population, together with the 1σ uncertainty band. We found that this source class might account for 0.13%–0.02% of the measured integrated flux of the IDGRB from 100 MeV. At the peak located at about 2 GeV, the MSPs contribute at most 0.9% to the spectra of the IDGRB. We notice that we shrink the uncertainty on this contribution to be $\mathcal{O}(10)$.

The observed *Fermi*-LAT and ATNF MSP height distributions differ significantly in the inner part of the Galaxy ($z \leqslant$ 0.3 kpc), because the sources detected in the radio band are more numerous than the γ-ray counterparts. It is demonstrated in this paper that the discrepancy is fully explained by the role of the LAT sensitivity at low latitudes.

Given the distribution of MSPs, which predicts that they are more abundant in the innermost part of the Galaxy, we may expect a non-negligible contribution of the unresolved population to the γ-ray emission at low latitudes. Moreover, close to the galactic disk the number of young pulsars overcomes that of MSPs. We have therefore considered both young and millisecond pulsar populations in order to assess the total γ-ray emission at low latitudes. The young pulsar population was modeled by following the method used for MSPs: we derived the distributions for radial and vertical distances, spin period, and surface magnetic field from the data of the ATNF catalog, and we relied on the 2FPC for the computation of best-fit γ-ray spectral parameters. We then derived the γ-ray emission from the unresolved young pulsars and MSPs in the inner part of our Galaxy by analyzing the inner Galaxy and the galactic center regions, where recently an excess in the *Fermi* -LAT data was claimed by different groups (Hooper & Slatyer 2013; Gordon & Macias 2013; Abazajian et al. 2014). Going from the inner Galaxy to the galactic center, the contribution of young pulsars increase with respect to the MSPs. We find that the peak of the γ-ray emission (at 2 GeV) from the unresolved MSP (young pulsar) is 4.1×10^{-9} GeV cm^{-2} s^{-1} sr^{-1} (9.1×10^{-11} GeV cm^{-2} s^{-1} sr^{-1}) for the inner Galaxy, and 1.9×10^{-7} GeV cm^{-2} s^{-1} sr^{-1} (4.5×10^{-7} GeV cm^{-2} s^{-1} sr^{-1}) for the galactic center.

Moreover, we calculated the γ-ray anisotropy arising from this source class by presenting the 1σ upper limit on the angular power, C_P. The result is that MSPs cannot be a sizeable contributor to the γ-ray anisotropy measured by the LAT at $|b| > 30°$, which should therefore be dominated by other source classes (e.g., radio-loud AGNs; Di Mauro et al. 2014, in preparation).

We demonstrated that although the population model is still affected by several uncertainties, those systematics have a little impact on the final prediction of the γ-ray flux from unresolved MSPs.

We acknowledge S. Ando, G. Bertone, and P. D. Serpico for a careful reading of the manuscript and useful comments. F.C. acknowledges support from the European Research Council through the ERC starting grant WIMPs Kairos, PI: G. Bertone. This work is supported by the research grant *TAsP (Theoretical Astroparticle Physics)* funded by the Istituto Nazionale di Fisica Nucleare (INFN), by the *Strategic Research Grant: Origin and Detection of Galactic and Extragalactic Cosmic Rays* funded by Torino University and Compagnia di San Paolo. At LAPTh this activity was supported by the Labex grant ENIGMASS.

APPENDIX

DISCUSSION OF SYSTEMATIC UNCERTAINTIES

As stressed in the text, the final results depend on how the MSP population has been built up (i.e., on the choices of the parameters characterizing the distributions assumed to model the source population). We dedicate this Appendix to the discussion of the systematic uncertainties affecting the results, showing how the diffuse emission at high latitudes changes when other distributions are assumed.

First, we discuss how the final spectrum is altered when assuming different choices for the magnetic field B, period P, and spatial radial r distributions. The results are displayed by Figure 14. For each varied parameter we derive the corresponding contribution to the diffuse emission as the average over 1000 MC realizations. The top left panel shows the impact of assuming different values of $\langle \log_{10}(B/G) \rangle$ for the magnetic field distribution of Equation (5). The cases with $\langle \log_{10}(B/G) \rangle = 8$ and $\langle \log_{10}(B/G) \rangle = 8.5$ are displayed. The integrated flux in the 0.1–100 GeV band is, respectively, about twice and a factor of 0.7 of the best-fit realization. The corresponding spectra are displayed in the panel together with the 1σ uncertainty band. In the top right panel, the reader can see how the choice of a power-law distribution for the rotation period P in the form $N(P) \propto P^{-\alpha}$ (with $\alpha = 2$), as assumed by Siegal-Gaskins et al. (2011), Grégoire & Knödlseder (2013), and Faucher-Giguère &

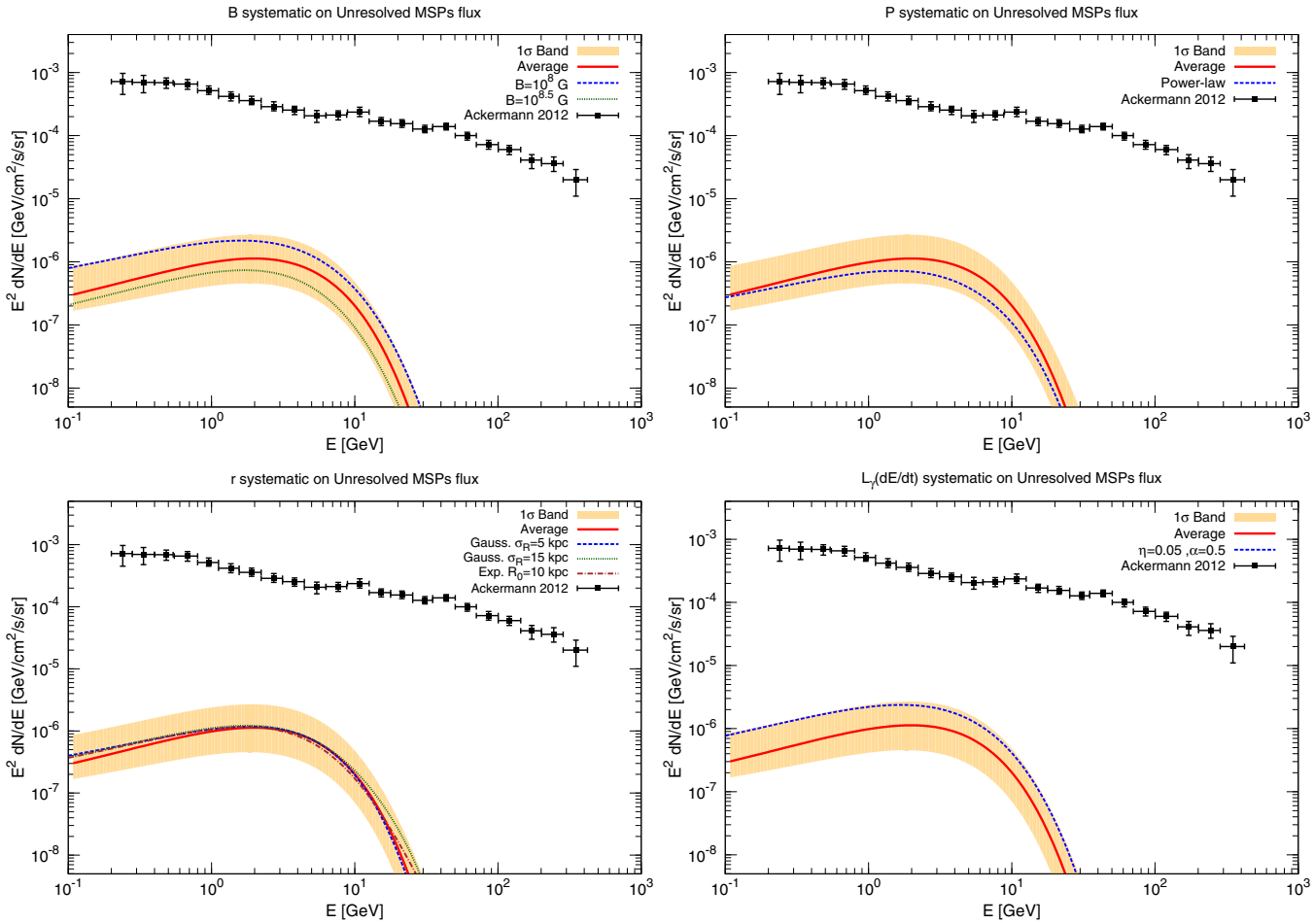

Figure 14. Systematic uncertainty on the MSP IDGRB flux is quantified, from the top left to the bottom right panels, by varying the assumption on the distributions for the magnetic field value, the period P distribution, the galactic distance of the galactic plane r distributions, and on the correlation between L_γ and $\dot{E}$. In each figure the best-fit curve and the 1σ band of Figure 9 are shown along with the cases explained in the text.

(A color version of this figure is available in the online journal.)

Loeb (2010), only marginally affects the results. We also note that the final results are independent from the spatial (radial) distribution adopted; the bottom left panel shows that using a Gaussian distribution, Equation (11), with $\sigma_r = 5, 10, 15$ kpc or an exponential distribution, Equation (10), with $r_0 = 10$ kpc (from Grégoire & Knödlseder 2013), does not change the result, and we are still close to the best-fit spectrum. Therefore, varying the surface magnetic field, rotation period, and space distribution does not alter our conclusions, and in all cases the ensuing systematic uncertainty is inside the 1σ uncertainty band.

In Section 4.1, we discussed the criticality and uncertainty on the efficiency conversion of spin-down luminosity $\dot{E}$ into γ-ray luminosity. Several papers (Siegal-Gaskins et al. 2011; Grégoire & Knödlseder 2013; Faucher-Giguère & Loeb 2010; Abdo et al. 2013) quote as possible $L_\gamma - \dot{E}$ relation:

$$L_\gamma \propto \sqrt{\dot{E}}. \tag{A1}$$

We found that assuming this relation does not influence our final result as is evident from the bottom right panel of Figure 14.

REFERENCES

Abazajian, K. N., Agrawal, P., Chacko, Z., & Kilic, C. 2010, JCAP, 11, 41
Abazajian, K. N., Blanchet, S., & Harding, J. P. 2011, PhRvD, 84, 103007
Abazajian, K. N., Canac, N., Horiuchi, S., & Kaplinghat, M. 2014, PhRvD, 90, 023526
Abdo, A. A., Ackermann, M., Ajello, M., et al. 2010a, ApJ, 720, 435
Abdo, A. A., Ackermann, M., Ajello, M., et al. 2010b, PhRvL, 104, 101101
Abdo, A. A., Ackermann, M., Atwood, W. B., et al. 2009, ApJ, 699, 1171
Abdo, A. A., Ajello, M., Allafort, A., et al. 2013, ApJS, 208, 17
Ackermann, M. 2012, 4th Fermi Symposium, http://galprop.stanford.edu/resources.php
Ackermann, M., Ajello, M., Albert, A., et al. 2012a, PhRvD, 85, 083007
Ackermann, M., Ajello, M., Allafort, A., et al. 2012b, ApJ, 755, 164
Aharonian, F., Akhperjanian, A. G., Bazer-Bachi, A. R., et al. 2006, A&A, 457, 899
Ajello, M., Romani, R. W., Gasparrini, D., et al. 2014, ApJ, 780, 73
Ajello, M., Shaw, M. S., Romani, R. W., et al. 2012, ApJ, 751, 108
Alpar, M. A., Cheng, A. F., Ruderman, M. A., & Shaham, J. 1982, Natur, 300, 728
Backer, D. C., Kulkarni, S. R., Heiles, C., Davis, M. M., & Goss, W. M. 1982, Natur, 300, 615
Berezinsky, V., Gazizov, A., Kachelrieß, M., & Ostapchenko, S. 2011, PhLB, 695, 13
Bergström, L., Ullio, P., & Buckley, J. H. 1998, APh, 9, 137
Blasi, P., Gabici, S., & Brunetti, G. 2007, IJMPA, 22, 681
Bringmann, T., Calore, F., Di Mauro, M., & Donato, F. 2014, PhRvD, 89, 023012
Brunthaler, A., Reid, M. J., Menten, K. M., et al. 2011, AN, 332, 461
Burgay, M., Keith, M. J., Lorimer, D. R., et al. 2013, MNRAS, 429, 579
Calore, F., De Romeri, V., Di Mauro, M., et al. 2014, MNRAS, 442, 1151
Calore, F., de Romeri, V., & Donato, F. 2012, PhRvD, 85, 023004
Cholis, I., Hooper, D., & McDermott, S. D. 2014, JCAP, 1402, 014
Cordes, J. M., & Chernoff, D. F. 1997, ApJ, 482, 971
Cuoco, A., Komatsu, E., & Siegal-Gaskins, J. 2012, PhRvD, 86, 063004
Di Mauro, M., Calore, F., Donato, F., Ajello, M., & Latronico, L. 2014a, ApJ, 780, 161

Di Mauro, M., Donato, F., Lamanna, G., Sanchez, D., & Serpico, P. 2014b, ApJ, 786, 129
Faucher-Giguere, C.-A., & Kaspi, V. M. 2006, ApJ, 643, 332
Faucher-Giguère, C.-A., & Loeb, A. 2010, JCAP, 1, 5
Fichtel, C. E., Hartman, R. C., Kniffen, D. A., et al. 1975, ApJ, 198, 163
Fornasa, M., Zavala, J., Sánchez-Conde, M. A., et al. 2013, MNRAS, 429, 1529
Gillessen, S., Eisenhauer, F., Trippe, S., et al. 2009, ApJ, 692, 1075
Gordon, C., & Macias, O. 2013, PhRvD, 88, 083521
Górski, K. M., Hivon, E., Banday, A. J., et al. 2005, ApJ, 622, 759
Grégoire, T., & Knödlseder, J. 2013, A&A, 554, A62
Hooper, D., Cholis, I., Linden, T., Siegal-Gaskins, J. M., & Slatyer, T. R. 2013, PhRvD, 88, 083009
Hooper, D., & Slatyer, T. R. 2013, PDU, 2, 118
Inoue, Y. 2011, ApJ, 733, 66
Johnson, T. J., Venter, C., Harding, A. K., et al. 2014, ApJS, 213, 6
Kalashev, O. E., Semikoz, D. V., & Sigl, G. 2009, PhRvD, 79, 063005
Keith, M., Johnston, S., Bailes, M., et al. 2011, arXiv:1109.4193
Kerr, M., & Fermi-LAT Collaboration. 2013, in IAU Symp. 291, Neutron Stars and Pulsars: Challenges and Opportunities after 80 years, ed. J. van Leeuwen (Cambridge: Cambridge Univ. Press), 307
Kraushaar, W. L., Clark, G. W., Garmire, G. P., et al. 1972, ApJ, 177, 341
Lange, C., Camilo, F., Wex, N., et al. 2001, MNRAS, 326, 274
Levin, L., Bailes, M., Barsdell, B., et al. 2013, arXiv:1306.4190
Lorimer, D., Faulkner, A., Lyne, A., et al. 2006, MNRAS, 372, 777
Lorimer, D. R. 2012, in Proc. of the IAU, Vol. 8, Neutron Stars and Pulsars; Changes and Opportunities After 80 years, ed. J. van Leeuwen (Cambridge: Cambridge Univ. Press), 237
Lorimer, D. R., & Kramer, M. 2004, Handbook of Pulsar Astronomy (Cambridge: Cambridge Univ. Press)
Lyne, A. G. 2000, RSPTA, 358, 831
Lyutikov, M., Otte, N., & McCann, A. 2012, ApJ, 754, 33
Magic Collaboration. 2011, ApJ, 742, 43
Magic Collaboration. 2012, A&A, 540, A69
Manchester, R. N., Hobbs, G. B., Teoh, A., & Hobbs, M. 2005, AJ, 129, 1993
McMillan, P. J., & Binney, J. J. 2010, MNRAS, 402, 934
Ng, C. Y., Takata, J., Leung, G., Cheng, K., & Philippopoulos, P. 2014, ApJ, 787, 167
Siegal-Gaskins, J. M., Reesman, R., Pavlidou, V., Profumo, S., & Walker, T. P. 2011, MNRAS, 415, 1074
Sreekumar, P., Bertsch, D. L., Dingus, B. L., et al. 1998, ApJ, 494, 523
Story, S. A., Gonthier, P. L., & Harding, A. K. 2007, ApJ, 671, 713
Tamborra, I., Ando, S., & Murase, K. 2014, JCAP, 1409, 043
Taylor, J. H., & Cordes, J. M. 1993, ApJ, 411, 674
Usov, V. V. 1983, Natur, 305, 409
VERITAS Collaboration. 2011, Sci, 334, 69
Yuan, Q., & Zhang, B. 2014, JHEAp, 3, 1
Yusifov, I., & Kucuk, I. 2004, A&A, 422, 545